Journal of Sound and Vibration (2000) **237**(5), 837–873
doi:10.1006/jsvi.2000.3147, available online at http://www.idealibrary.com on IDEAL®

NON-LINEAR COUPLED TRANSVERSE AND AXIAL VIBRATION OF A COMPLIANT STRUCTURE, PART 1: FORMULATION AND FREE VIBRATION

S. M. Han and H. Benaroya

Mechanical and Aerospace Engineering, Rutgers, the State University of New Jersey, Piscataway, NJ 08854, *U.S.A.*

(*Received* 28 *October* 1999, *and in final form* 5 *June* 2000)

A compliant tower in the ocean environment is modelled as a beam undergoing coupled transverse and axial motion. The equations of motion are non-linear and coupled and are derived here. The beam is assumed to be supported by a linear-elastic torsional spring at one end and with a point mass at the other end. Such a model is representative of numerous applications. The equations of motion and boundary conditions are obtained using Hamilton's variational principle. It is assumed that strains are small but the rotation is moderate compared to the strain so that the equations of motion for the axial and transverse motion are non-linearly coupled. The free response in vacua and the free response in water are considered in particular. The fluid forces, the added mass and drag forces, are modelled using a semi-empirical Morison equation. The resulting non-linear coupled partial differential equations are solved numerically using the finite difference approach. In Part 2 of this work, various forced responses are studied.

1. INTRODUCTION

Offshore structures are used in the oil industry as exploratory, production, oil storage, and oil landing facilities. In general, there are two types of offshore structures. They are fixed and compliant structures. Fixed structures are designed to withstand environmental forces without any substantial displacement. Therefore, a linear dynamic analysis may be sufficient. Compliant structures are designed to allow small but not negligible deformation and deflection. Tension, provided by a large buoyancy chamber, makes the structure stable. For these structures, the dynamic responses may have non-linear characteristics which need to be explored fully.

Fixed structures become impractical for deep water because they must be built stronger and more bulky than the equivalent compliant structures. In recent years, the need to explore deeper water has made compliant structures more popular.

An articulated tower includes a ballast chamber near the bottom, a buoyancy chamber near the surface of the water, and a shaft that connects them as shown in Figure 1. The tower is connected to its base by a universal joint that allows the tower to move in all directions. A tension leg platform is vertically moored by a tendon at each corner of the platform as shown in Figure 2. Buoyancy is provided by the pontoon that is submerged in the fluid.

A vertical member of an offshore structure may be modelled as a beam undergoing extension and bending. Such members are the shaft of an articulated tower and tendons of a tension leg platform.

0022-460X/00/450837 + 37 $35.00/0

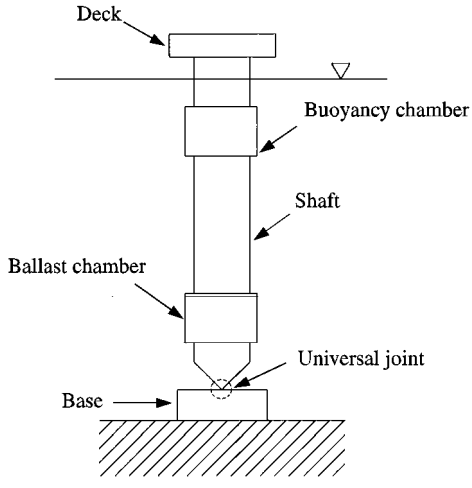

Figure 1. Schematic of an articulated tower.

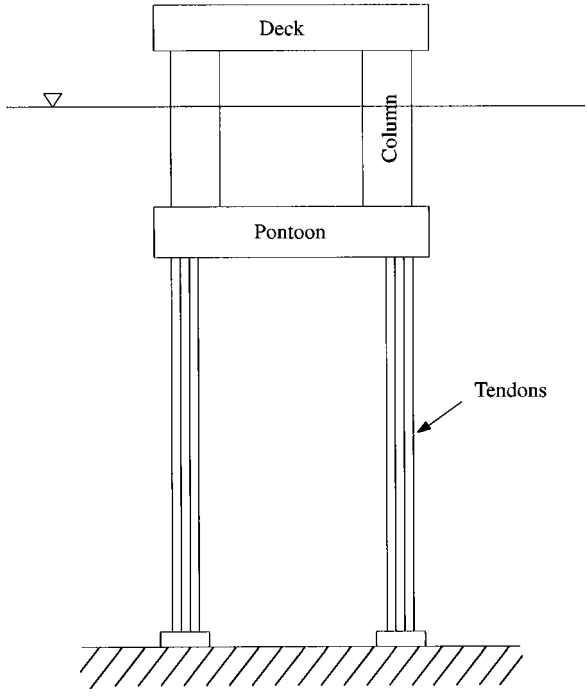

Figure 2. Schematic of a tension leg platform.

An articulated tower or a tension leg platform can be modelled as a beam with a linear-elastic torsional spring at its base and a concentrated mass at its free tip as shown in Figure 3. The vertical member such as a shaft of an articulated tower or tendons of a tension leg platform is modelled as a beam. The torsional spring simulates the various support conditions from hinged to clamped by varying the spring constants from zero to infinity. The point mass is representative of structures supported by the shaft or tendons.

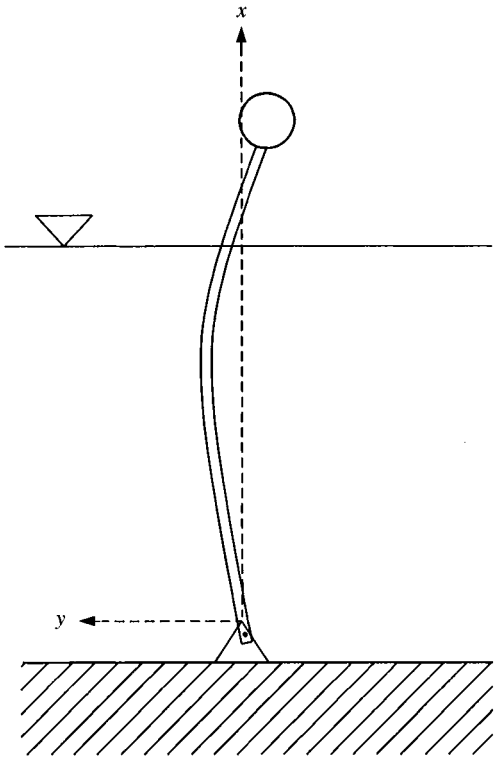

Figure 3. A beam supported by a torsional spring.

In our, model, the structure is confined to a plane. Motion in the third direction, out of page in Figure 3, is not allowed. The reader is referred to an extensive review of non-linear dynamics of compliant towers which can be found in the paper by Adrezin *et al.* [1].

In linear behavior, transverse and longitudinal motion are decoupled and can be described effectively by simple linear partial differential equations: extensional motion by

$$EA_o \frac{\partial^2 u(x,t)}{\partial x^2} = \rho A_o \frac{\partial^2 u(x,t)}{\partial t^2} \tag{1}$$

and transverse motion by

$$EI_o \frac{\partial^4 v(x,t)}{\partial x^4} = -\rho A_o \frac{\partial^2 v(x,t)}{\partial t^2}, \tag{2}$$

where $u(x, t)$ is the axial deflection, $v(x, t)$ is the transverse deflection, E is Young's modulus, A_o is the cross-sectional area, I_o is the area moment of inertia of the cross-section around the neutral axis, and ρ is the material density. The linear model for transverse vibration, equation (2), is called the Euler–Bernoulli model.

For a vibrating beam, the rigid-body motion and bending are the primary components of the overall behavior. Therefore, it may be sufficient to use a single-degree-of-freedom model (s.d.o.f.) or a linear transverse model such as Euler–Bernoulli, Rayleigh, shear or Timoshenko model. A discussion of linear transverse models can be found in the paper by Han *et al.* [2]. The linear transverse models assume that the coupling between the

transverse and the axial motion is negligible. However, the coupling becomes more significant with increasing slenderness ratio (the ratio of length to the radius of gyration of the cross-sectional area). Therefore, the non-linear coupling effect in long slender members of compliant towers may be important in an overall response.

The purpose of this paper is to formulate the non-linear equations of motion for the coupled transverse and longitudinal vibration (section 2), to formulate the environmental forces imposed by still water (section 3), and to present and analyze the free and damped free motion (section 4). Part 2 of this work contains studies of forced vibration.

2. MATHEMATICAL MODEL OF THE STRUCTURE

The displacement field is obtained under the assumptions of Kirchhoff's hypothesis. It is also assumed that the strain is small but the rotation is moderate compared to the strain. This assumption introduces a non-linearity to the system model. The strains that correspond to the displacement field are obtained. The stresses are obtained from strains using constitutive relations that ignore the Poisson effect. The strain energy is then obtained. The equations of motion and the corresponding boundary conditions are then obtained using Hamilton's principle.

2.1. DISPLACEMENTS, STRAINS, AND STRESSES

Let us consider a beam with an original length L. Beam elements are labelled by their location in the undeformed configuration, X. The reference and current configurations of the midplane are shown in Figure 4. The dotted line is the reference configuration, and the solid line is the current configuration.

Using Kirchhoff's hypothesis, we write the displacements as

$$u_1(X, Y, t) = u(X, t) - Y \frac{\partial v}{\partial X}(X, t),$$

$$u_2(X, t) = v(X, t), \qquad u_3(X, t) = 0, \tag{3}$$

where u is the deflection of the midplane in the x direction and v in the y direction. Y is the transverse distance from the midplane to the point of interest on the cross-section in the reference frame. Assuming a symmetrical cross-section, u is also the average deflection of the beam element X. We assume that the strain is small, but the rotation can be moderate. Mathematically, we write

$$\frac{\partial u_1}{\partial X} \sim \left(\frac{\partial u_2}{\partial X}\right)^2 \ll 1. \tag{4}$$

In terms of midplane deflections, we can write

$$\frac{\partial u}{\partial X} \sim \left(\frac{\partial v}{\partial X}\right)^2 \ll 1. \tag{5}$$

It should be noted that in order for Kirchhoff's hypothesis to be valid, the only condition that has to be satisfied is that the strains be small when compared to the rotation [3]. Therefore, by using Kirchhoff's hypothesis, we have already assumed small strains and moderate rotation.

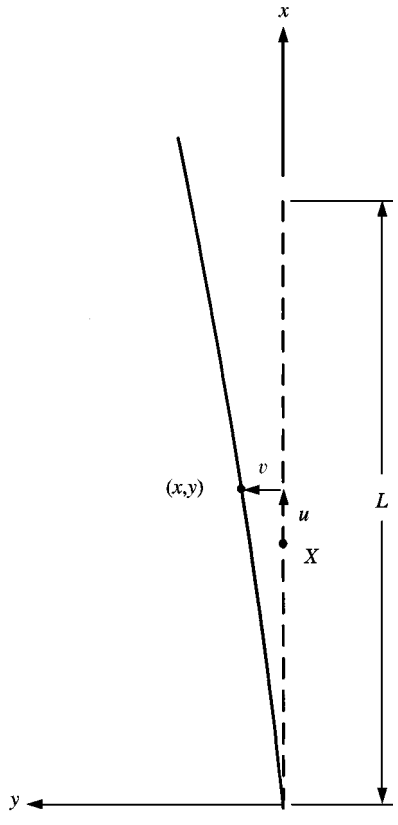

Figure 4. The reference and current midplane configurations of the beam.

With this assumption, Green's strains are given by

$$\mathscr{E}_{XX} = \frac{\partial u_1}{\partial X} + \frac{1}{2}\left(\frac{\partial u_2}{\partial X}\right)^2, \quad \mathscr{E}_{YY} = \frac{\partial u_1}{\partial Y}, \quad \mathscr{E}_{XY} = \frac{1}{2}\left[\frac{\partial u_2}{\partial X} + \frac{\partial u_1}{\partial Y}\right], \quad \mathscr{E}_{YZ} = 0, \qquad \mathscr{E}_{XZ} = 0,$$

$$\mathscr{E}_{ZZ} = 0. \tag{6}$$

Using the assumed displacement field given in equation (3), Green's strains are given by

$$\mathscr{E}_{XX} = \frac{\partial u}{\partial X} - Y\frac{\partial^2 v}{\partial X^2} + \frac{1}{2}\left(\frac{\partial v}{\partial X}\right)^2, \quad \mathscr{E}_{YY} = 0, \qquad \mathscr{E}_{XY} = 0, \tag{7}$$

where we keep in mind that u and v are functions of X and t.

The second Kirchhoff stress, ignoring the Poisson effect, is given by

$$\tilde{\sigma}_{XX} = E\mathscr{E}_{XX}. \tag{8}$$

2.2. LAGRANGIAN

The general expression for the strain energy is given by

$$PE_{strain} = \frac{1}{2}\int_{V_o} \tilde{\sigma}_{ij}\mathscr{E}_{ij}\,\mathrm{d}V_o, \tag{9}$$

where V_o is the volume of the undeformed beam. Using the expressions for the second Kirchhoff stress and Green's strain, we obtain

$$PE_{strain} = \frac{E}{2}\int_X \int_{A_o} \left(u' - Yv'' + \frac{1}{2}v'^2\right)^2 \mathrm{d}A_o\,\mathrm{d}X, \tag{10}$$

where prime notation is used for derivatives with respect to X. Expanding the integrand, we obtain

$$PE_{strain} = \frac{E}{2}\int_0^L \int_{A_o} \left(u'^2 - 2u'v''Y + v'^2u' + Y^2v''^2 - v'^2Yv'' + \frac{1}{4}v'^4\right)\mathrm{d}A_o\,\mathrm{d}X. \tag{11}$$

Integrating over the area, the terms that are odd functions of Y (second and fifth) disappear due to symmetric cross-section, and Y^2 becomes the area moment of inertia I_o about the neutral axis. The rest are functions of X and t only.

The potential energy stored in the torsional spring is given by

$$PE_{spring} = \tfrac{1}{2}k\theta^2, \tag{12}$$

where θ is the angle of twist of the torsional spring. The angle of twist, θ, can be approximated by the first derivative of the transverse deflection $v'(0, t)$ using the small-angle assumption.

Therefore, we can write the potential energy as

$$PE = \frac{1}{2}\int_0^L \left[EA_o\left(u' + \frac{1}{2}v'^2\right)^2 + EI_o v''^2\right]\mathrm{d}X + \frac{1}{2}kv'(0, t)^2. \tag{13}$$

The kinetic energy has two components: kinetic energy of the beam and kinetic energy of the point mass. The kinetic energy of the beam is given by

$$KE_{beam} = \frac{1}{2}\int_0^L \int_{A_o} [\rho(\dot{u}_1^2 + \dot{u}_2^2)]\,\mathrm{d}A_o\,\mathrm{d}X, \tag{14}$$

where dot notation is used for derivatives with respect to time. Replacing the axial displacement u_1 and u_2 using equation (3), we can write

$$\begin{aligned}\frac{\rho}{2}\int_0^L \int_{A_o} (\dot{u}_1^2 + \dot{u}_2^2)\,\mathrm{d}A_o\,\mathrm{d}X &= \frac{\rho}{2}\int_0^L \int_{A_o} [(\dot{u} - Y\dot{v}')^2 + \dot{v}^2]\,\mathrm{d}A_o\,\mathrm{d}X \\ &= \frac{\rho}{2}\int_0^L \int_{A_o} (\dot{u}^2 - 2Y\dot{u}\dot{v}' + Y^2\dot{v}'^2 + \dot{v}^2)\,\mathrm{d}A_o\,\mathrm{d}X \\ &= \frac{1}{2}\int_0^L [\rho A_o(\dot{u}^2 + \dot{v}^2) + \rho I_o\dot{v}'^2]\,\mathrm{d}X,\end{aligned} \tag{15}$$

where the term with factor Y integrated over the cross-section disappeared and the term with factor Y^2 integrated over the cross-section became I_o as before. The kinetic energy of

the point mass is given by

$$KE_{point\ mass} = \tfrac{1}{2} M_p[\dot{v}^2(L, t) + \dot{u}^2(L, t)]. \tag{16}$$

The kinetic energy of the system is written as

$$KE = \frac{1}{2}\int_0^L [\rho A_0(\dot{u}^2 + \dot{v}^2) + \rho I_o \dot{v}'^2]\,\mathrm{d}X + \frac{1}{2} M_p[\dot{v}^2(L, t) + \dot{u}^2(L, t)]. \tag{17}$$

The term $\rho I_o \dot{v}'^2$ is Rayleigh's rotational term. It is the kinetic energy due to the rotation of the cross-section and is usually small compared to the kinetic energy due to translation, $\rho A_o(\dot{u}^2 + \dot{v}^2)$.

The Lagrangian integrated over time, $\int_{t_i}^{t_f} \mathscr{L}\,\mathrm{d}t = \int_{t_i}^{t_f} (KE - PE)\,\mathrm{d}t$, is given by

$$\begin{aligned}\int_{t_i}^{t_f} \mathscr{L}\,\mathrm{d}t &= \frac{1}{2}\int_{t_i}^{t_f}\left\{\int_0^L\left[\rho A_o(\dot{u}^2 + \dot{v}^2) + \rho I_o \dot{v}'^2 - EA_o\left(u' + \frac{1}{2}v'^2\right)^2 - EI_o v''^2\right]\mathrm{d}X\right.\\ &\left. + \frac{1}{2} M_p[\dot{v}^2(L, t) + \dot{u}^2(L, t)] - \frac{1}{2} k v'^2(0, t)\right\}\mathrm{d}t\end{aligned} \tag{18}$$

and the virtual work done by transverse and axial forces is given by

$$\delta W = \int_0^L (f(X, t)\delta v + p(X, t)\delta u)\,\mathrm{d}X. \tag{19}$$

2.3. EQUATIONS OF MOTION AND BOUNDARY CONDITIONS VIA HAMILTON'S PRINCIPLE

The variation of equation (18) is given by

$$\begin{aligned}\delta\int_{t_i}^{t_f} \mathscr{L}\,\mathrm{d}t = \int_{t_i}^{t_f}\left\{\int_0^L\right.\Big[&\rho A_o(\dot{u}\,\delta\dot{u} + \dot{v}\,\delta\dot{v}) + \rho I_o \dot{v}'\,\delta\dot{v}'\\ &- EA_o\left(u' + \frac{1}{2}v'^2\right)(\delta u' + v'\,\delta v') - EI_o v''\,\delta v''\Big]\mathrm{d}X\\ &\left. + M_p[\dot{v}(L, t)\,\delta\dot{v}(L, t) + \dot{u}(L, t)\,\delta\dot{u}(L, t)] - k v'(0, t)\,\delta v'(0, t)\right\}\mathrm{d}t.\end{aligned} \tag{20}$$

Integrating by parts, we obtain

$$\begin{aligned}\delta\int_{t_i}^{t_f} \mathscr{L}\,\mathrm{d}t = \int_{t_i}^{t_f}\Bigg[&\left\{\int_0^L\left\{-\rho A_o\ddot{u} + \left[EA_o\left(u' + \frac{1}{2}v'^2\right)\right]'\right\}\delta u\right.\\ &\left. + \left\{-\rho A_o\ddot{v} + \left(EA_o\left(u' + \frac{1}{2}v'^2\right)v'\right)' + \rho I_o\ddot{v}'' - (EI_o v'')''\right\}\delta v\,\mathrm{d}X\right]\mathrm{d}t\end{aligned}$$

$$+\int_{t_i}^{t_f}\left\{\left[(\mathrm{E}I_o v'')' - \rho I_o \ddot{v}' - EA_o\left(u' + \frac{1}{2}v'^2\right)v'\right]\delta v\right\}\Big|_0^L \mathrm{d}t$$

$$+\int_{t_i}^{t_f}\left\{-EA_o\left(u' + \frac{1}{2}v'^2\right)\delta u - EI_o v''\,\delta v'\right\}\Big|_0^L \mathrm{d}t$$

$$-\int_{t_i}^{t_f} M_p[\ddot{v}(L,t)\,\delta v(L,t) + \ddot{u}(L,t)\,\delta u(L,t)]\,\mathrm{d}t$$

$$+\int_{t_i}^{t_f} kv'(0,t)\,\delta v'(0,t)\,\mathrm{d}t. \tag{21}$$

Note that the variations at the two endpoints in time are assumed to be zero. Hamilton's principle states that $\delta\int_{t_i}^{t_f}(\mathscr{L} + W)\,\mathrm{d}t = 0$, and thus the non-linear coupled equations of motion are given by

$$\rho A_o \ddot{u} - \left(EA_o\left(u' + \frac{1}{2}v'^2\right)\right)' = p,$$

$$\rho A_o \ddot{v} - \left(EA_o\left(u' + \frac{1}{2}v'^2\right)v'\right)' - (\rho I_o \ddot{v}')' + (EI_o v'')'' = f \tag{22}$$

and the corresponding boundary conditions are given by

$$EA_o\left(u' + \frac{1}{2}v'^2\right)\delta u\Big|_0^L + M_p\ddot{u}(L,t)\,\delta u(L,t) = 0,$$

$$\left[(EI_o v'')' - \rho I_o \ddot{v}' - EA_o\left(u' + \frac{1}{2}v'^2\right)v'\right]\delta v\Big|_0^L - M_p\ddot{v}(L,t)\,\delta v(L,t) = 0,$$

$$EI_o v''\,\delta v'|_0^L + kv'(0,t)\,\delta v'(0,t) = 0. \tag{23}$$

For the problem at hand, the boundary conditions are given by

$$u(0,t) = 0, \quad \left[EA_o\left(u' + \frac{1}{2}v'^2\right) + M_p\ddot{u}\right]\Big|_{L,t} = 0,$$

$$v(0,t) = 0, \quad kv' - EI_o v''|_{0,t} = 0,$$

$$\left[(EI_o v'')' - \rho I_o \ddot{v}' - EA_o\left(u' + \frac{1}{2}v'^2\right)v' - M_p\ddot{v}\right]\Big|_{L,t} = 0,$$

$$EI_o v''(L,t) = 0. \tag{24}$$

Note that similar equations of motion and boundary conditions are obtained by Bottega [4], Yigit and Christoforou [5], and Adrezin [6, 7]. Also note that Adrezin uses the Eulerian formulation instead of the Lagrangian formulation used in this paper.

2.4. NON-DIMENSIONALIZATION

Now, let us non-dimensionalize our equations of motion. The length scales X, $v(X, t)$, $u(X, t)$ are normalized by the length of the beam L, the time t is normalized by $1/\bar{\omega}$ where $\bar{\omega}$ is some characteristic angular frequency. The energy is normalized by the bending energy. We find that the equations of motion are then given by

$$\bar{m}\frac{\partial^2 \bar{u}}{\partial \bar{t}^2} - \frac{\partial}{\partial \bar{x}}\left(s^2\left(\frac{\partial \bar{u}}{\partial \bar{x}} + \frac{1}{2}\left(\frac{\partial \bar{v}}{\partial \bar{x}}\right)^2\right)\right) = \bar{p},$$

$$\bar{m}\frac{\partial^2 \bar{v}}{\partial \bar{t}^2} - \frac{\partial}{\partial \bar{x}}\left(s^2\left(\frac{\partial \bar{u}}{\partial \bar{x}} + \frac{1}{2}\left(\frac{\partial \bar{v}}{\partial \bar{x}}\right)^2\right)\frac{\partial \bar{v}}{\partial \bar{x}}\right) - \frac{\partial}{\partial \bar{x}}\left(\bar{J}\frac{\partial^3 \bar{v}}{\partial \bar{t}^2\,\partial \bar{x}}\right) + \frac{\partial^4 \bar{v}}{\partial \bar{x}^4} = \bar{f}, \tag{25}$$

where barred quantities are non-dimensional quantities. Their expressions are given by

$$\bar{m} = \rho A\frac{\bar{\omega}^2 L^4}{EI}, \quad s^2 = \frac{L^2}{I/A}, \quad \bar{J} = \rho I\frac{L^2\bar{\omega}^2}{EI},$$

$$\bar{p} = p\frac{L^3}{EI}, \quad \bar{f} = f\frac{L^3}{EI}, \quad \bar{M}_p = M_p\frac{\bar{\omega}^2 L^3}{EI}, \quad \bar{k} = k\frac{L}{EI}. \tag{26}$$

Note that the non-linear coupling terms in the equations of motion have an s^2 factor in common. s is the slenderness ratio, the ratio of the length of the beam to the radius of gyration of the cross-section. If the beam is slender, the contribution of the non-linear coupling term becomes large. Therefore, this non-linear coupling term may be important for offshore structures which tend to be long.

3. FORMULATION OF $p(X, t)$ AND $f(X, t)$

The external forcing functions, $f(X, t)$ and $p(X, t)$, are formulated to simulate forces when a beam is placed under water and under gravity. The axial force per unit length $p(X, t)$ is due to gravity and buoyancy and is given by

$$\begin{aligned} p(X, t) &= -\rho g A_o + \rho_f g A_f \quad \text{for } 0 < X < d \\ &= -\rho g A_o \quad \text{for } d < X < L, \end{aligned} \tag{27}$$

where ρ_f is the density of the surrounding fluid, g is the gravitational acceleration, A_f is the cross-section of the displaced volume πr_{outer}^2, d is the water depth, and L is the undeformed beam length.

The transverse force is formulated using the Morison equation, given by [8]

$$f(X, t) = -C_A\rho_f A_f\ddot{R}^n + C_M\rho_f A_f\dot{U}^n + C_D\rho_f r_{outer}V_{rel}^n|V_{rel}^n|, \tag{28}$$

where R is the displacement of the beam, $\dot{U}$ is the acceleration of the fluid, and V_{rel} is the relative velocity of fluid with respect to the structure. The superscript n is used to indicate that they are normal components (normal to the structure). C_A is the added mass coefficient, C_D is the drag coefficient, and C_M is the inertia coefficient. Note that the Morison equation is applicable when the drag force is predominant, which is the case when the structural diameter is small compared to the water wavelength [9].

The first term in equation (28) is the added mass term, the second is the inertial term, and the third is the drag term. The added mass effect is due to the fact that some of the fluid

particles are displaced by the motion of the cylinder. The inertia force is exerted by the fluid when it accelerates and decelerates as it passes around the circular cylinder. It also can be interpreted as the force required to hold a cylinder stationary in a flow of uniform acceleration. The drag force is due to the pressure difference between the downstream and upstream region. Since we assume, in the initial part of this study, that the water is still, there is no inertia force and the relative velocity of the fluid with respect to the structure is the negative of the structural velocity. In vectorial form, we can write the velocity and the acceleration of the structure as

$$\dot{\mathbf{R}} = -\mathbf{V}_{rel} = \dot{u}\mathbf{i} + \dot{v}\mathbf{j}, \qquad \ddot{\mathbf{R}} = \ddot{u}\mathbf{i} + \ddot{v}\mathbf{j}. \tag{29}$$

The normal components can be obtained by performing the double cross-products

$$\ddot{R}^n = |\mathbf{1} \times \ddot{\mathbf{R}} \times \mathbf{1}|, \qquad V_{rel}^n = |\mathbf{1} \times \mathbf{V}_{rel} \times \mathbf{1}|, \tag{30}$$

where the tangent vector $\mathbf{1}$ (to the structure) is given by

$$\mathbf{1} = \mathbf{i} + v'\mathbf{j} \tag{31}$$

and it is assumed that the angle of rotation is negligible when compared to 1. The resulting normal vectors are given by

$$\ddot{R}^n = -\ddot{u}v' + \ddot{v}, \qquad V_{rel}^n = \dot{u}v' - \dot{v}. \tag{32}$$

Finally, the transverse force is given by

$$f(X, t) = -C_A \rho_f A_f(-\ddot{u}v' + \ddot{v}) + C'_D \rho_f r_{outer}(\dot{u}v' - \dot{v})|\dot{u}v' - \dot{v}|, \tag{33}$$

where C'_D is the drag coefficient for an oscillating cylinder in still water. The coefficient C'_D is different from C_D. The drag coefficient C'_D takes into account the velocity that occurs due to an oscillating cylinder.

4. RESULTS AND DISCUSSION

The responses are obtained numerically for a beam with the same physical parameters as one constructed by Professor Timothy Wei's group at Rutgers University. We hope to make comparisons with experiments to be carried out in the future. The beam and the fluid properties are given in Tables 1 and 2.

TABLE 1

The beam properties

Beam properties	
Material	Aluminum
Young's modulus, E	73·0 GPa
Density, ρ	2770 kg/m^3
Point mass, M_p	0·236 kg
Torsional spring constant, k	38·8 N/m
Length, L	1·27 m
Outer radius, r_o	0·0127 m
Inner radius r_i	0·0101 m

TABLE 2

The fluid properties

Fluid properties	
Density of water, ρ_f	999 kg/m^3
Water depth, d	1·05 m
Added mass coefficient, C_A	1
Modified drag coefficient, C'_D	1

First, we consider a uniform beam vibrating freely in vacuum in a gravity-free environment. This will provide us with the non-linear structural characteristics such as frequencies and shapes of free response. Second, we consider a beam vibrating in still water under gravity. The Morison equation with damping and added mass terms is used to simulate this condition. This will provide us with the damped characteristics such as the frequencies and shapes of oscillation of the damped response. In both cases, free and damped–free, the beam will oscillate due to non-zero initial conditions: initial displacement and/or initial velocity.

Non-linearities can influence the response in many ways. For example, the frequencies of vibration may vary with the initial conditions and vibration amplitude whereas those are constant quantities in linear systems. Let us consider four initial conditions in order to demonstrate the sensitivity to these. Here, we assume that the initial velocity is zero and the displacement fields correspond to physical configurations shown in Figure 5.

The four sets of initial displacements are listed in Table 3. The parameters (point loads and applied moment) are chosen such that the static transverse end deflection is 0·05 m, which is approximately 4% of the beam length. The corresponding axial end deflections are about 0·001 m for IC_1 and IC_3 and 0·002 m for IC_2. These end deflections may be seen in the experiments and is small enough so that the small-angle assumption is valid.

The finite difference approach is employed to obtain the responses. The finite difference equations are written for the spatial derivatives for N nodes leading to the equations of motion in terms of $2N$ second order ordinary differential equations in time. MATLAB function ode45.m is used to solve the resulting ordinary differential equations. The function ode45.m solves ordinary differential equations with initial conditions using the fourth or fifth order Runge–Kutta method. Between 8 and 30 nodes are used initially to determine the fewest number of nodes that can be used to ensure convergence. Here, 14 nodes are used. It was found that the response obtained using 14 and 30 nodes do not deviate significantly from each other.

The natural frequencies predicted by the linear models of equations (1) and (2), with appropriate boundary conditions, are given in Table 4. These data will be useful for comparisons and discussions when we obtain the frequencies of vibration for the non-linear system. The physical configuration that is used for the linear longitudinal model is a beam that is fixed at one end and has a point mass at the other end. The physical configuration for the linear transverse model is a beam that is supported by a torsional spring at one end and has a point mass at the other end.

The corresponding initial transverse displacements that can be used for the linear transverse model are given in Table 5.

This is a study preliminary to the forced response due to random waves and current. When the current is added to the system, we expect to see a non-zero equilibrium position after the transient response has died out. When the random waves are added to the Morison

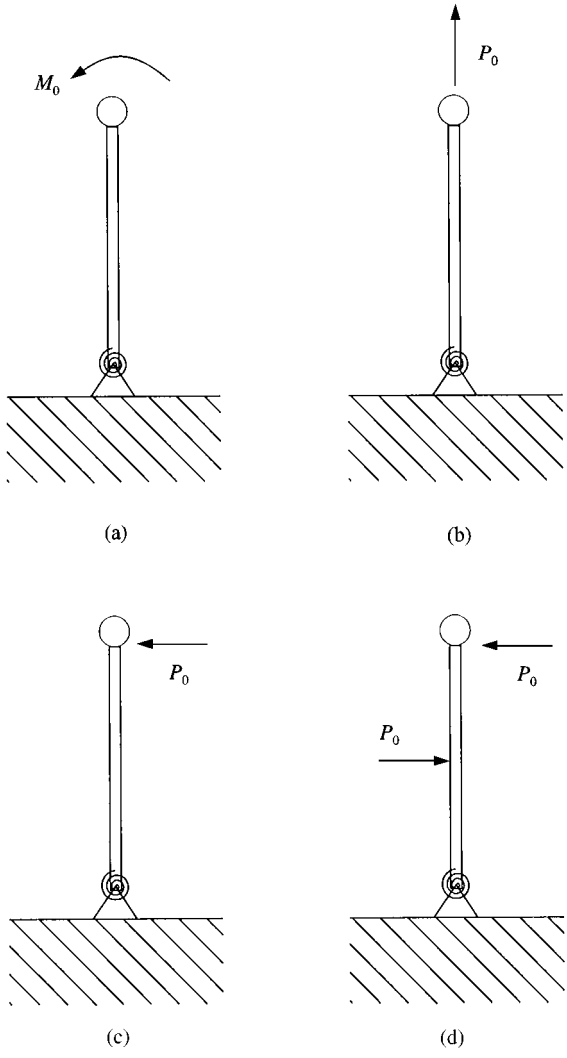

Figure 5. Four sets of initial displacements.

equation, the system will respond at additional frequencies. These cases are discussed in Part 2.

4.1. THE FREE RESPONSE

In this section, we consider the free response of the system in vacuum and in a gravity-free environment. We first look at the displacements at the tip, and corresponding phase plots and spectral density plots. In addition, the physical elongation is plotted so that the axial displacement is not mistaken as the elongation of the beam. The potential and kinetic energies are plotted. From these studies, we hope to gain some insights to the physical system such as the interaction between the axial and transverse displacements, the natural frequencies of the system, and the distribution of energies within the system.

TABLE 3

Four sets of initial displacements

IC_1

$$u(X,0) = -\frac{1}{2}\left(\frac{P_o}{EI}\right)^2\left(\frac{X^5}{20} - \frac{LX^4}{4} + \left(L^2 - \frac{EIL}{k}\right)\frac{X^3}{3} + \frac{EIL^2X^2}{k} + \left(\frac{EIL}{k}\right)^2 X\right)$$

$$v(X,0) = -\frac{P_o}{EI}\left(\frac{X^3}{6} - \frac{LX^2}{2} - \frac{EILX}{k}\right)$$

IC_2

$$u(X,0) = -\frac{1}{2}\left(\frac{M_o}{EI}\frac{X^3}{3} + \frac{M_o^2}{EIk}X^2 + \frac{M_o^2}{k^2}X\right)$$

$$v(X,0) = M_o\left(\frac{X^2}{2EI} + \frac{X}{k}\right)$$

IC_3

$$u(X,0) = P_o^2L^2\left[\frac{X^3}{48(EI)^2} + \frac{X^2}{16EIk} + \frac{x}{16k^2}\right] \quad \text{for } 0 < X \leqslant \frac{L}{2}$$

$$u(X,0) = \left(\frac{P_o}{2EI}\right)^2\left[\frac{X^5}{20} - \frac{LX^4}{4} + \left(\frac{3L^2}{8} - \frac{LEI}{6k}\right)X^3 - \left(\frac{L^2}{8} - \frac{LEI}{2k}\right)LX^2 + \left(\frac{L^2}{8} - \frac{LEI}{2k}\right)^2 X\right] \quad \text{for } \frac{L}{2} < X < L$$

$$v(X,0) = \frac{P_oL}{2}\left(\frac{X^2}{2EI} + \frac{X}{k}\right) \quad \text{for} \quad 0 < X < \frac{L}{2}$$

$$v(X,0) = -\frac{P_o}{EI}\left(\frac{X^3}{6} - \frac{LX^2}{2} + \left(\frac{LEI}{2k} - \frac{L^2}{8}\right)X - \frac{L^3}{48}\right) \quad \text{for } \frac{L}{2} < X < L$$

IC_4

$$u(X,0) = \frac{P_o}{EA_o}X$$

$$v(X,0) = 0$$

TABLE 4

The natural frequencies obtained using linear models

Linear longitudinal model (Hz)	Linear transverse model (Hz)
$f_{u1} = 677{\cdot}65$	$f_{v1} = 1{\cdot}2337$
$f_{u2} = 2313{\cdot}7$	$f_{v2} = 47{\cdot}549$
$f_{u3} = 4190{\cdot}6$	$f_{v3} = 172{\cdot}728$

4.1.1. *The displacements, phase plots, and spectral density plots for the free end motion*

This is the case where the external forcing functions, $p(X,t)$ and $f(X,t)$, equal zero in equation (22). Figures 6–9 show the responses of the beam when subjected to initial conditions IC_1 to IC_4 in Table 3. There are four plots in each figure. They are the tip displacements versus time and phase plots for the tip. The plots in the left column are for the axial vibration and those in the right column are for the transverse vibration.

Let us look at the responses when the first three sets of initial conditions are used. From the displacement plots, we notice that the motions in both transverse and axial direction

TABLE 5

Four sets of initial displacements for linear model

IC_1	$v(X,0) = -\dfrac{P_o}{EI}\left(\dfrac{X^3}{6} - \dfrac{LX^2}{2} - \dfrac{EILX}{k}\right)$
IC_2	$v(X,0) = -M_o\left(\dfrac{X^2}{2EI} + \dfrac{X}{k}\right)$
IC_3	$v(X,0) = \dfrac{P_o L}{2}\left(\dfrac{X^2}{2EI} + \dfrac{X}{k}\right)$ for $0 < X < \dfrac{L}{2}$
	$v(X,0) = -\dfrac{P_o}{EI}\left(\dfrac{X^3}{6} - \dfrac{LX^2}{2} + \dfrac{L}{8k}(Lk - 4EI)X + \dfrac{L^3}{48}\right)$ for $\dfrac{L}{2} < X < L$

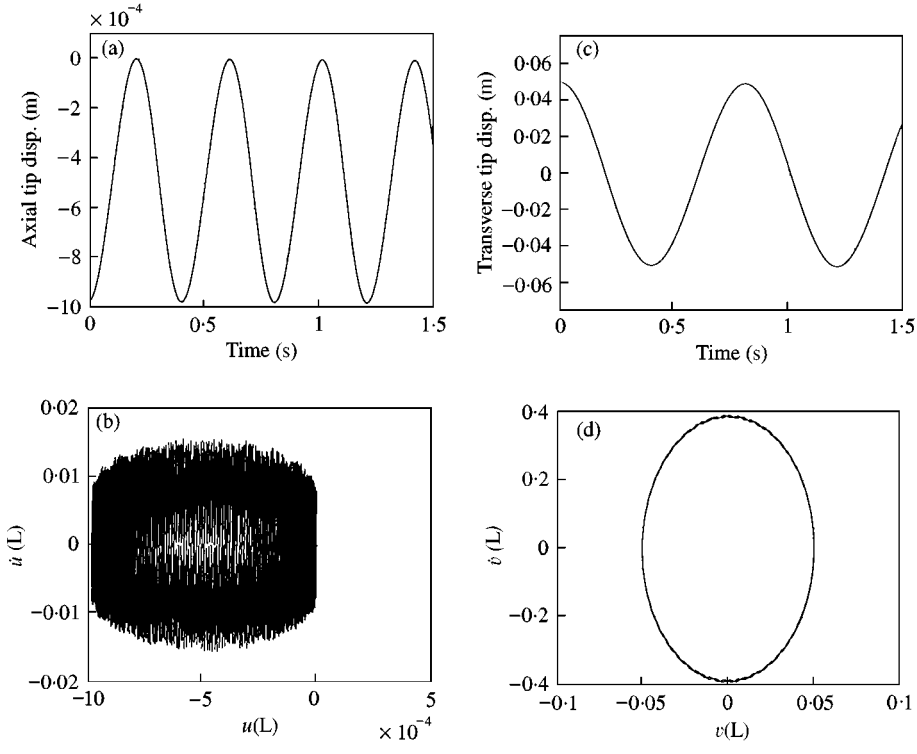

Figure 6. The free response plots using IC_1: (a) axial tip displacement versus time, (b) phase plot for the tip axial motion, (c) transverse tip displacement versus time, (d) phase plot for the tip displacement motion.

look sinusoidal. Only the axial displacement in Figure 7(a) seems to have a high-frequency component. However, the phase plots for all three cases show the high-frequency component, which indicates that all responses have high-frequency components and only the amplitude of the high-frequency component varies from case to case. The low-frequency or the fundamental frequency component describes the dominant motion or an envelop which can be seen easily in the displacement plots.

Now, let us look at the transverse displacement plots in Figures 6(c)–8(c). They are shown superimposed in Figure 10. We find from the figures that the period for the transverse

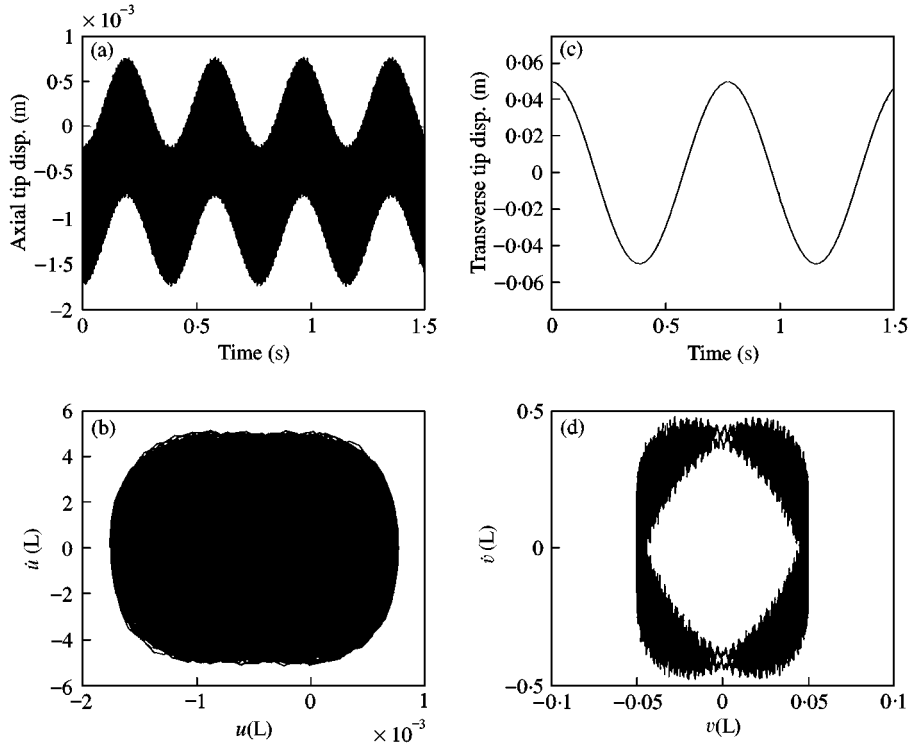

Figure 7. The free response plots using IC_2: (a) axial tip displacement versus time, (b) phase plot for the tip axial motion, (c) transverse tip displacement versus time, (d) phase plot for the tip transverse motion.

response is about 0·81 s (1·23 Hz) when IC_1 and IC_3 are used. This frequency is close to the one predicted by the linear model. The period for the transverse responses are about 0·74 s (1·35 Hz) when IC_2 is used. These fundamental frequencies of the transverse motion varied with initial conditions, which is a characteristic of a non-linear system.

The transverse tip displacements shown in Figures 8(c)–10(c) are plotted again in Figure 11 against the transverse tip displacements obtained using the linear model. The responses look similar except for when IC_2 is used.

Figure 12 shows the spectral density plots of axial and transverse motion when IC_2 is used. The frequency at which the peaks occur are f_u = 2·6, 47·3, 678, 2307, … (Hz), f_v = 1·3, 47·3, 170, 317, 361 508, 622, 630, 678, 725, 848, 931, 1273, 1631, 1988, 2138, 2307, … (Hz). Comparing the frequencies obtained using the linear models in Table 4, we find that the frequencies 678 and 2307 Hz for the axial vibration and 1·3, 47·3, and 170 Hz can be found approximately using the linear models. The rest can only be obtained using the non-linear model.

Note that the fundamental frequencies of the axial motion are twice those of transverse vibration. In order to explain why this is the case, let us look at a typical path taken by the free end of the beam shown in Figure 13. When the free end goes through points 1, 2 and 3, the transverse displacement makes half a cycle while the axial displacement makes one complete cycle. This is true even when there is no longitudinal strain. Therefore, the fundamental frequency in the axial displacement is purely due to the geometry. The tip transverse displacement $v(L, t)$ is plotted in Figure 14 against the axial tip displacement

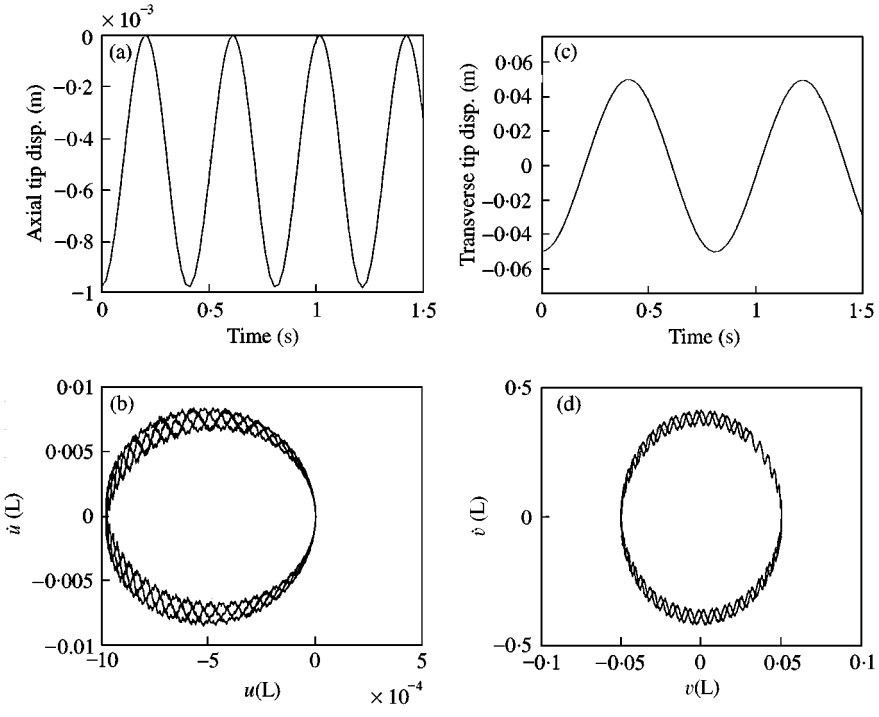

Figure 8. The free response plots using IC_3: (a) axial tip displacement versus time, (b) phase plot for the tip axial motion, (c) transverse tip displacement versus time, (d) phase plot for the tip transverse motion.

$u(L, t)$ when IC_1 is used. The shape describes the actual path taken by the free end. The schematic in Figure 13 indeed resembles the actual path.

In order to explain analytically why the fundamental frequency of the axial motion is twice that of the transverse motion, let us go back to the axial equation of motion in equation (22) with $p(x, t) = 0$, or

$$\rho A_o \ddot{u} - EA_o u'' = EA_o v' v''. \tag{34}$$

From the response plots, we know that the transverse motion is approximately sinusoidal with frequency ω_v. Then we can say v is approximately given by

$$v \approx g(X) e^{i\omega_v t}. \tag{35}$$

Therefore, we can think of equation (34) as being forced by $EA_o g'(X) g''(X) e^{i(2\omega_v)t}$ which has a frequency of $2\omega_v$. Therefore, the solution of equation (34) has frequencies that are natural frequencies of the linear model (solution of $\rho A_o \ddot{u} - EA_o u'' = 0$) and the forcing frequency $2\omega_v$.

Let us look at the response plots in Figure 9 when fourth initial condition is used. Recall that this is the case when there is an axial initial displacement only. The response plots show that the transverse displacement stays zero. This shows that it is possible to excite the axial motion without affecting the transverse motion. Physically, it is possible to have longitudinal stress without generating moments. On the other hand, the reverse is not true. It is not possible to have moments without generating longitudinal stress. Therefore, it is

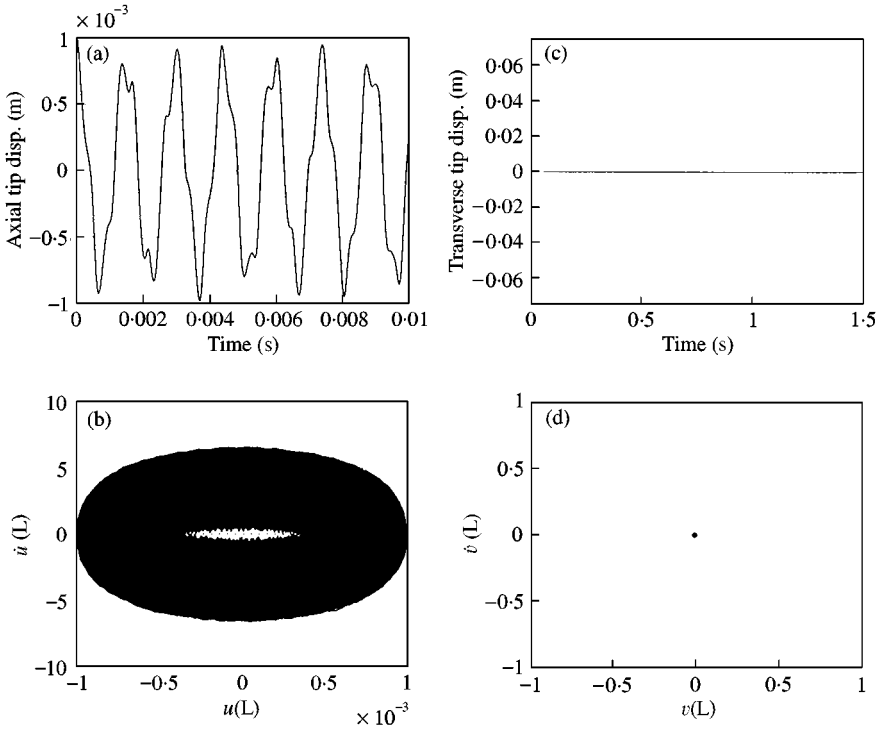

Figure 9. The free response plots using IC_4: (a) axial tip displacement versus time, (b) phase plot for the tip axial motion, (c) transverse tip displacement versus time, (d) phase plot for the tip transverse motion.

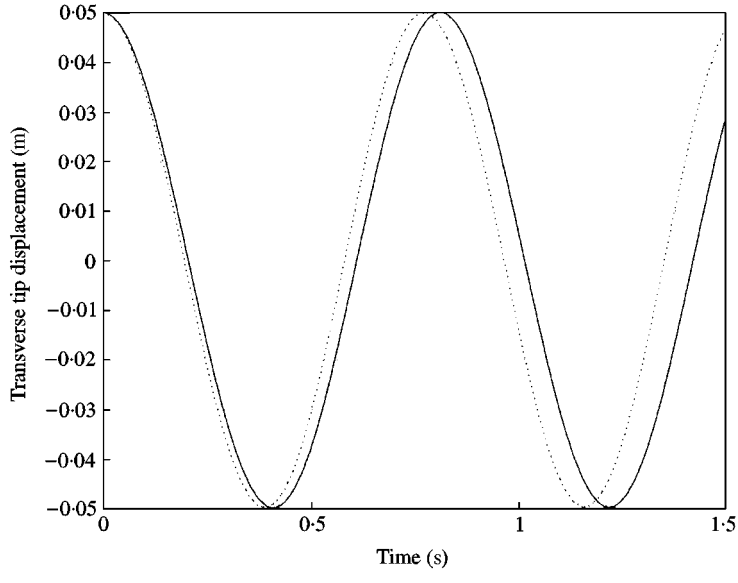

Figure 10. Transverse tip displacements of the free vibrations: —, IC_1; ·····, IC_2; –·– IC_3.

not possible to excite the transverse motion without affecting the axial motion. The axial motion in this case can be described by the linear longitudinal model given by

$$\rho A_o \ddot{u} - EA_o u'' = 0. \tag{36}$$

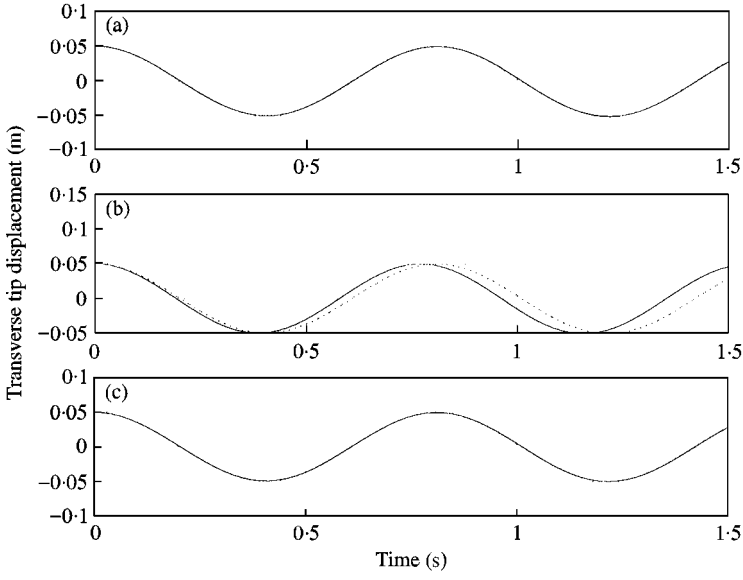

Figure 11. Transverse tip displacement obtained using both linear and nonlinear models: (a) IC_1, (b) IC_2, (c) IC_3: —, non-linear; ·····, linear model.

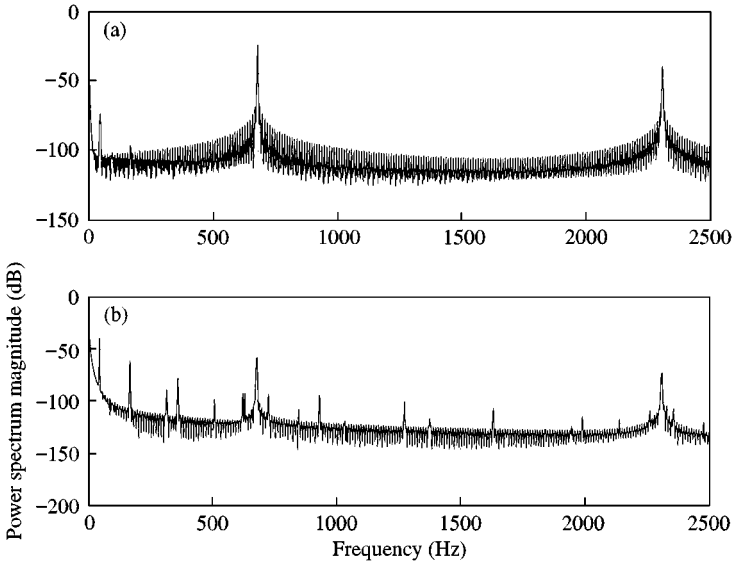

Figure 12. The power spectral density plots using IC_2: (a) axial motion, (b) transverse motion.

It should be noted that the axial displacement does not give any information on the longitudinal strain nor the physical elongation of the beam directly. Figure 15 shows the elongation of the beam as a function of time for all four cases. The expression for the elongation $\mathrm{d}\Delta$ of a beam element shown in Figure 16 is given by

$$\mathrm{d}\Delta = \sqrt{[\mathrm{d}X + u(X + \mathrm{d}X) - u(X)]^2 + [v(X + \mathrm{d}X) - v(X)]^2} - \mathrm{d}X. \tag{37}$$

Sum of these $\mathrm{d}\Delta$ gives the total elongation of the beam.

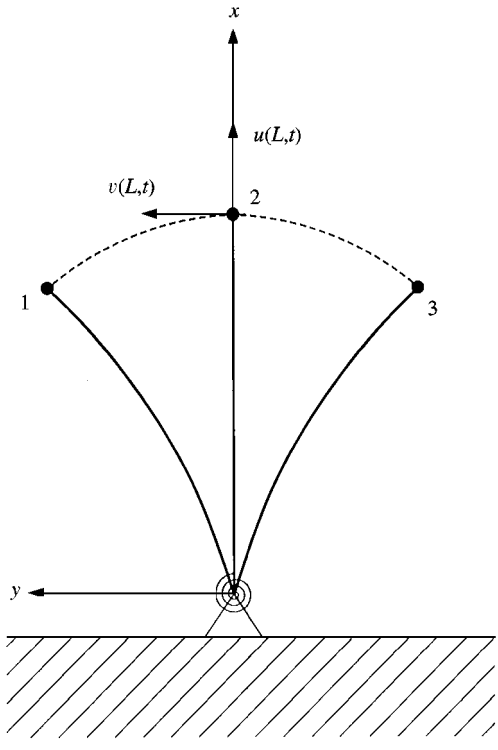

Figure 13. A typical path taken by the free end.

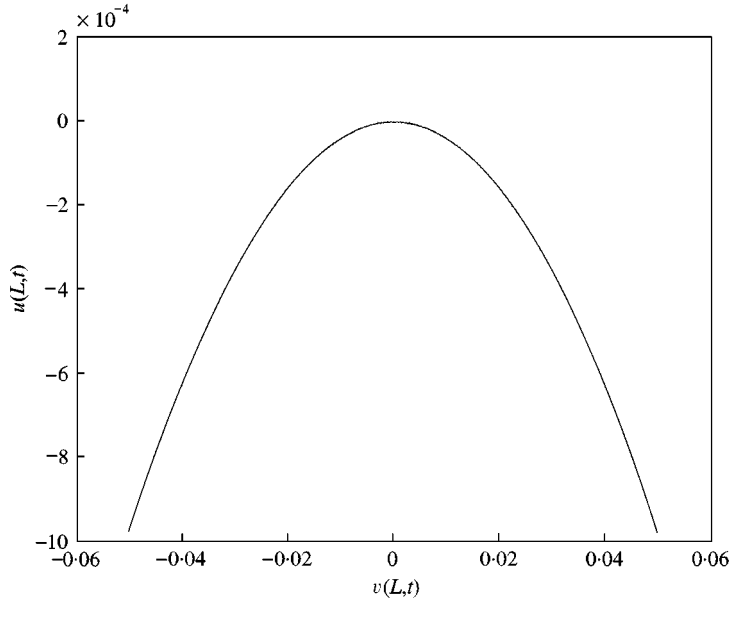

Figure 14. $v(L, t)$ versus $u(L, t)$ using IC_1.

The elongations for all cases are mostly positive. The shapes do not resemble sinusoidal functions. Instead, peaks tend to be sharper when the beam is at the extreme position. Figure 17 shows the power spectral density plot of the elongation of the beam

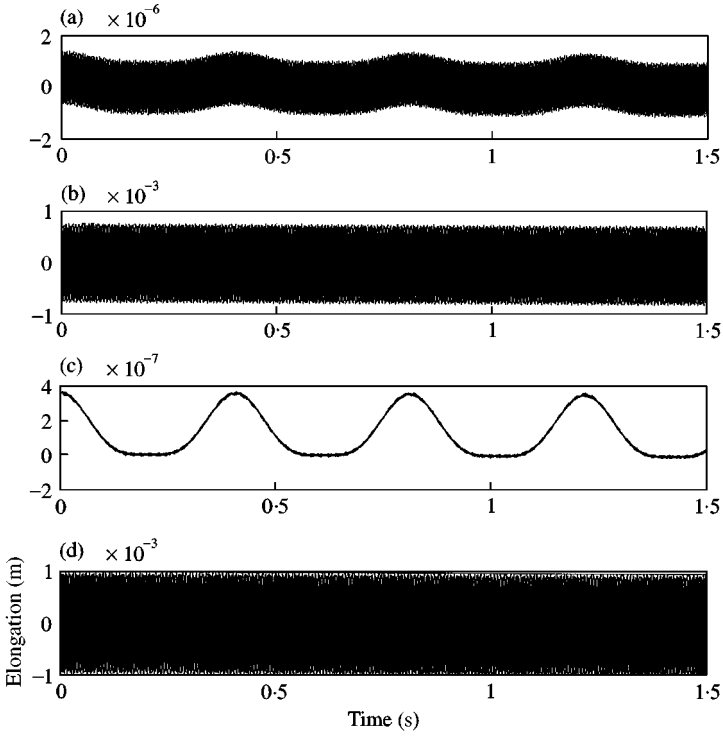

Figure 15. The elongation versus time for the free response using four sets of initial conditions: (a) IC_1, (b) IC_2, (c) IC_3, (d) IC_4. (The high frequency is at 678 Hz).

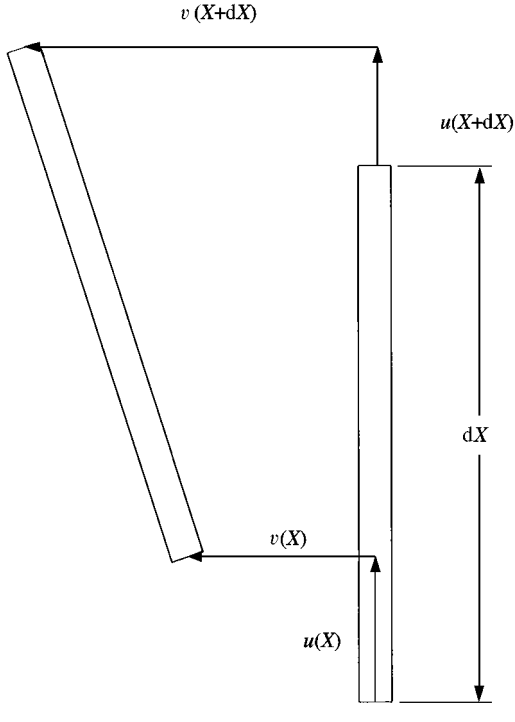

Figure 16. A beam element.

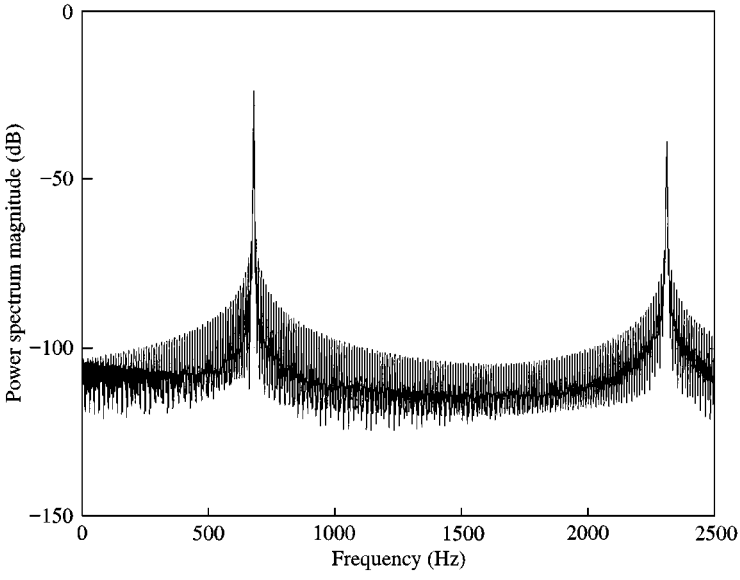

Figure 17. The power spectral density plot of elongation using IC_2.

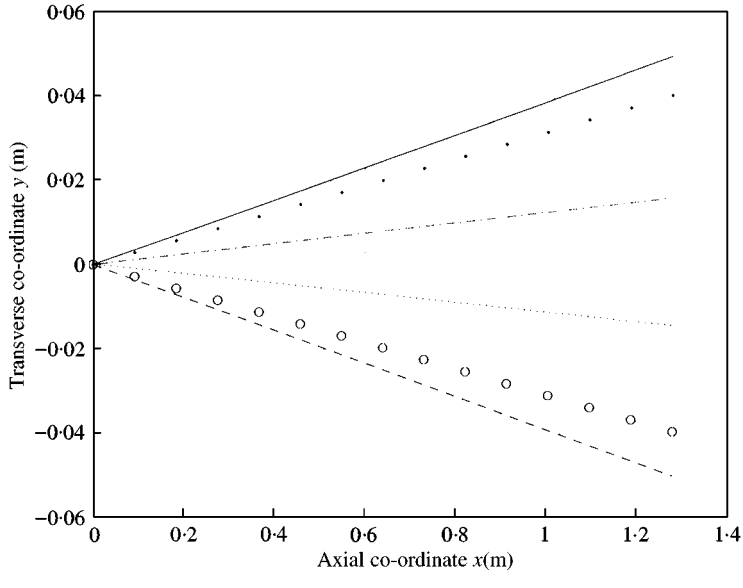

Figure 18. The free response at 0·08 second interval: —, $t = 0$; ·····, $t = 0{\cdot}08$, – · –, $t = 0{\cdot}16$; · · · · ·, $t = 0{\cdot}24$; ◦ ◦, $t = 0{\cdot}32$; – –, $t = 0{\cdot}40$

for IC_2. Note that it resembles the power spectral density plot of the axial motion in Figure 14(a).

So far, we have only examined the tip responses (displacement and phase plots). It may be interesting to look at the whole beam at different times. Figure 18 shows the responses when IC_1 is used for the time from zero to 0·4 s at 0·05 s intervals. The beam goes through approximately a half cycle. We observe that the overall motion is similar to the first mode shape of the linear beam. Therefore, if we are concerned with the overall motion only,

discarding the small amplitude high-frequency component may be reasonable, and the linear model may be sufficient.

4.1.2. *The potential and kinetic energies*

So far, we have examined the tip displacements, phase plots for the free end, spectral density plots for the free end, and elongation of the beam. Next, we consider how the energy is distributed in order to understand the physical system better.

Figures 19–21 show the potential energies, and Figures 22–24 show the kinetic energies using the first three sets of initial conditions. The potential energies are the bending energy, membrane energy, and the potential energy stored in the torsional spring. Their expressions are given by

$$PE_{bending} = \frac{1}{2}\int_0^L EI_o v''^2 \, \mathrm{d}X,$$

$$PE_{membrane} = \frac{1}{2}\int_0^L EA_o\left(u' + \frac{1}{2}v'^2\right)^2 \mathrm{d}X, \quad PE_{spring} = \frac{1}{2}kv'(0,t)^2. \tag{38}$$

The kinetic energies are the translational kinetic energy of the beam, rotational kinetic energy of the beam, and the translational kinetic energy of the point mass. Their expressions are given by

$$KE_{translation} = \frac{1}{2}\int_0^L \rho A_o(\dot{u}^2 + \dot{v}^2)\,\mathrm{d}X, \quad KE_{rotation} = \frac{1}{2}\int_0^L \rho I_o \dot{v}'^2 \,\mathrm{d}X,$$

$$KE_{point\ mass} = \frac{1}{2}M_p(\dot{v}(L,t)^2 + \dot{u}(L,t)^2). \tag{39}$$

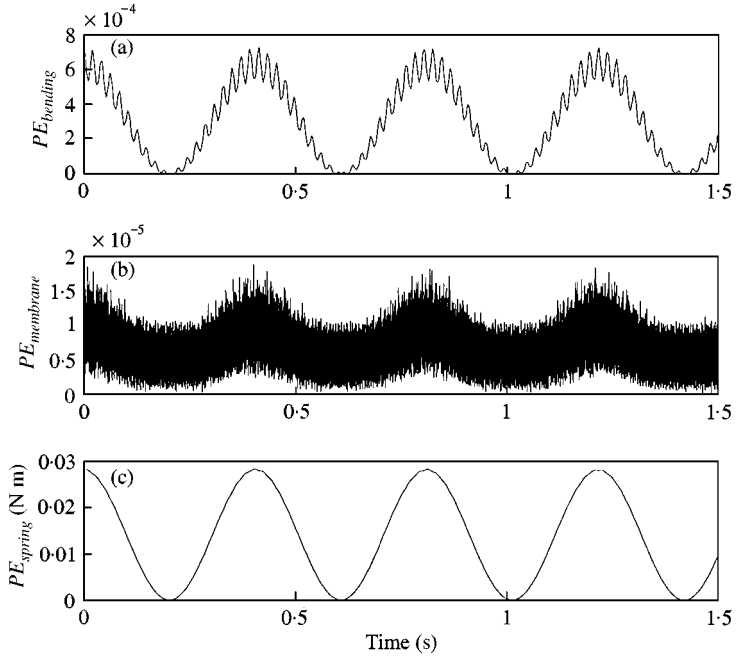

Figure 19. The potential energies of free vibration using IC_1: (a) $PE_{bending}$, (b) $PE_{membrane}$, (c) PE_{spring}.

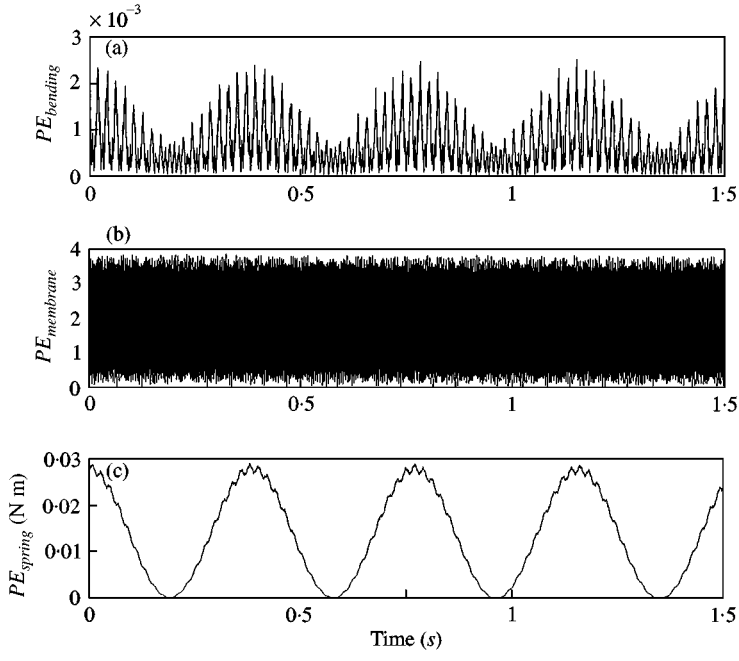

Figure 20. The potential energies of free vibration using IC_2: (a) $PE_{bending}$, (b) $PE_{membrane}$, (c) PE_{spring}.

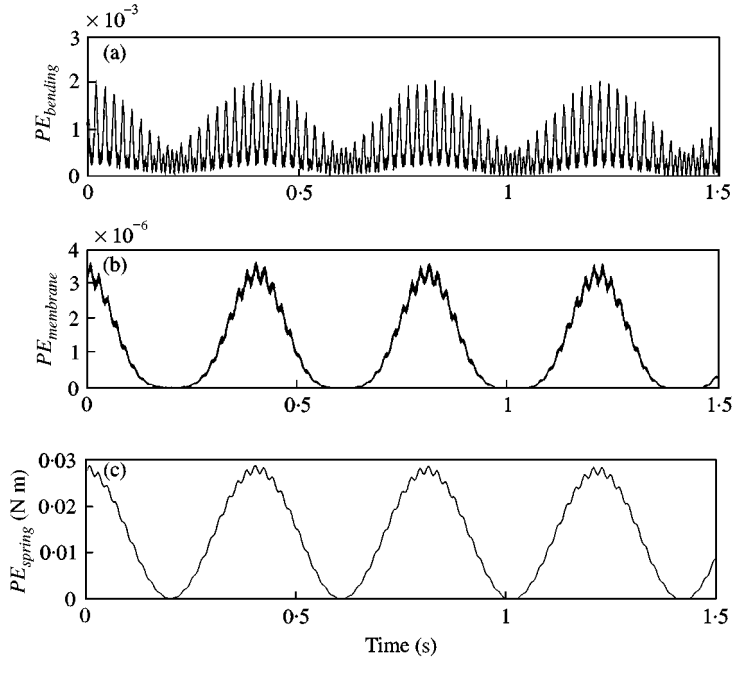

Figure 21. The potential energies of free vibration using IC_3: (a) $PE_{bending}$, (b) $PE_{membrane}$, (c) PE_{spring}.

From the energy plots, we observe that the magnitude of the high-frequency component varied from case to case. This was seen in the tip displacement plots in section 4.1.1.

The amplitudes of the potential energy stored in the torsional spring are almost the same for all three cases. Recall that the end deflections for all three cases are set to 0·05 m. The

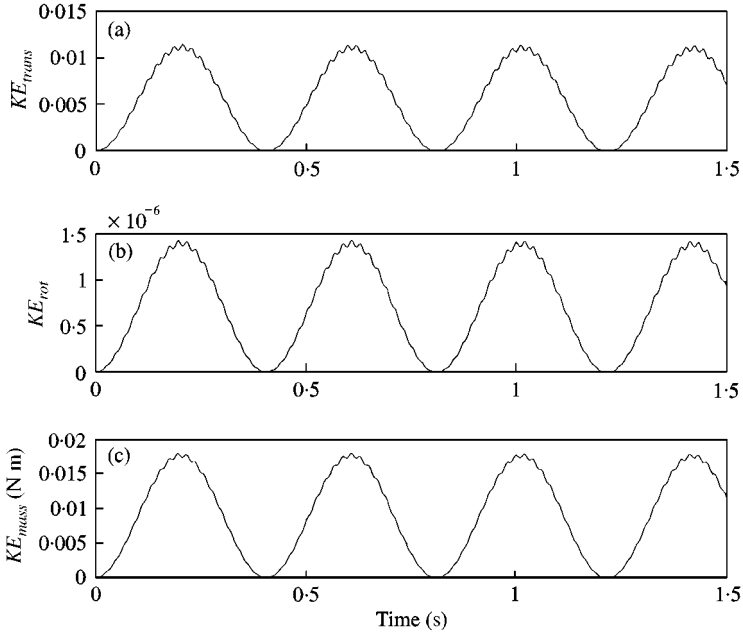

Figure 22. The kinetic energies of free vibration using IC_1: (a) $KE_{translation}$, (b) $KE_{rotation}$, (c) $KE_{point\ mass}$.

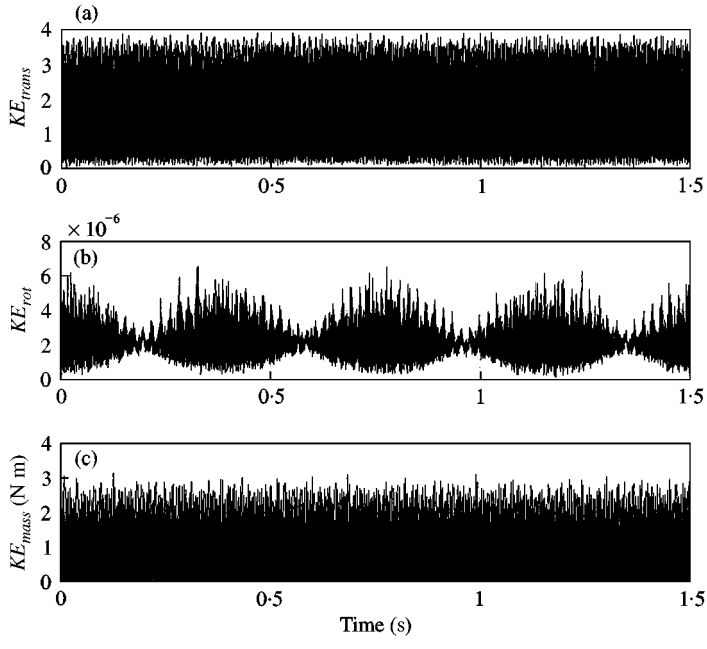

Figure 23. The kinetic energies of free vibration using IC_2: (a) $KE_{translation}$, (b) $KE_{rotation}$, (c) $KE_{point\ mass}$.

beam is almost rigid in our case such that the initial deflections of the torsional spring, $v'(0, t)$, for all three cases are near $0{\cdot}05/L$. Therefore, it is reasonable that the energy stored in the spring are almost the same for all three cases. The potential energies are then distributed between the bending and the membrane energies. The bending energy is the dominant term

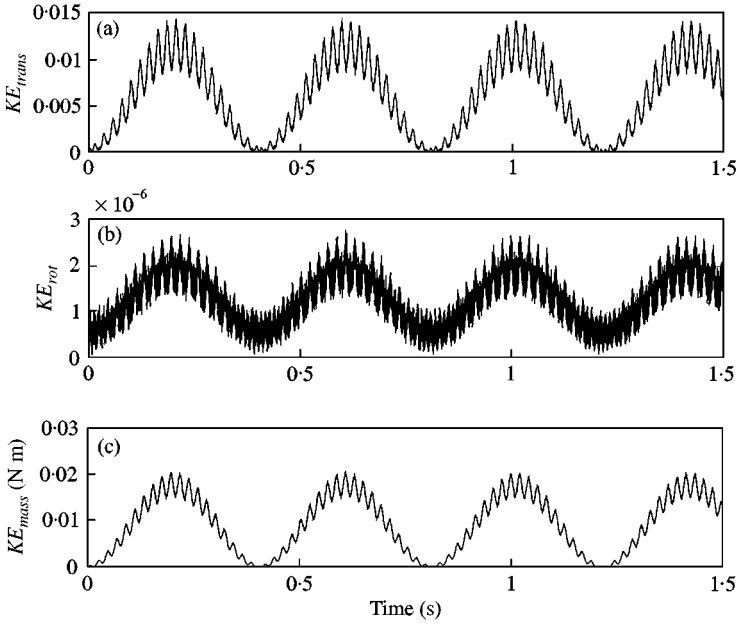

Figure 24. The kinetic energies of free vibration using IC_3: (a) $KE_{translation}$, (b) $KE_{rotation}$, (c) $KE_{point\ mass}$.

for IC_1 where the high-frequency extensional effects are small, and the membrane energy is the dominant term for IC_2 and IC_3 where the high-frequency extensional effects are significant.

Notice the similarity between the shapes of the membrane energy and the elongation of the beam shown in Figure 15. This can be explained by rewriting the incremental elongation in equation (37) as

$$\mathrm{d}\Delta = \left[\sqrt{\left(1+\frac{\mathrm{d}u}{\mathrm{d}X}\right)^2+\left(\frac{\mathrm{d}v}{\mathrm{d}X}\right)^2}-1\right]\mathrm{d}X. \tag{40}$$

Using the Taylor expansion around $\mathrm{d}u/\mathrm{d}X \approx 0$ and $\mathrm{d}v/\mathrm{d}X \approx 0$, we can rewrite the incremental elongation as

$$\mathrm{d}\Delta = \left[\frac{\mathrm{d}u}{\mathrm{d}X}+\frac{1}{2}\left(\frac{\mathrm{d}v}{\mathrm{d}X}\right)^2+O\left(\left(\frac{\mathrm{d}u}{\mathrm{d}X}\right)^3+\left(\frac{\mathrm{d}v}{\mathrm{d}X}\right)^3\right)\right]\mathrm{d}X. \tag{41}$$

Assuming small strain and moderate rotation given in equation (5), we can write

$$\mathrm{d}\Delta \approx \left[\frac{\mathrm{d}u}{\mathrm{d}X}+\frac{1}{2}\left(\frac{\mathrm{d}v}{\mathrm{d}X}\right)^2\right]\mathrm{d}X. \tag{42}$$

This expression is seen in the membrane energy expression. Therefore, the membrane energy directly translates into the elongation of the beam. We also notice that the potential energy and the kinetic energy are 180° out of phase.

Figures 25 and 26 show the power spectral density plots of the potential and kinetic energy when IC_2 is used. The high frequency shown in $PE_{membrane}$, KE_{trans}, and KE_{mass} is

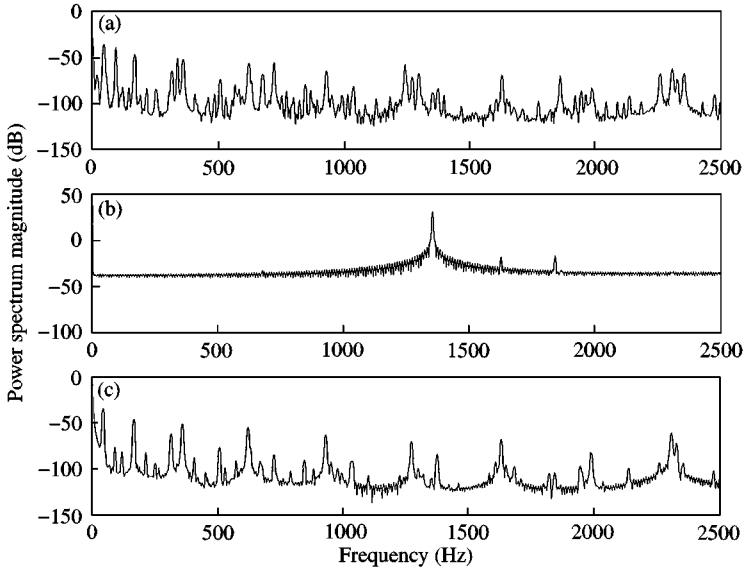

Figure 25. The power spectral density plots of potential energies using IC_2: (a) $PE_{bending}$, (b) $PE_{membrane}$, (c) PE_{spring}.

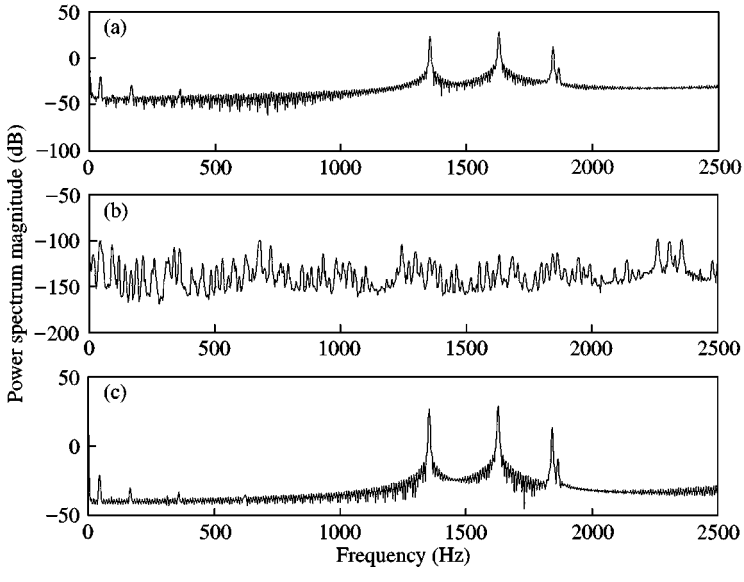

Figure 26. The power spectral density plots of kinetic energies using IC_2: (a) $KE_{translation}$, (b) $KE_{rotation}$, (c) $KE_{point\ mass}$.

1356 Hz. This is twice the frequency seen in the axial displacement. This makes sense because those energies are quadratic functions of $u(X, t)$ or derivatives of $u(X, t)$. The power spectral density plots for $PE_{bending}$, PE_{spring}, and $KE_{rotation}$ have many more peaks. This is because those energies are functions of $v(X, t)$ or derivatives of $v(X, t)$, which has many more peaks in their power spectral density plot.

Figure 27 shows the total energy of the system when IC_1 is used. The total energy is constant because the system is conservative. The total energies for IC_2 and IC_3 (not shown here) show more numerical errors, that grow with time.

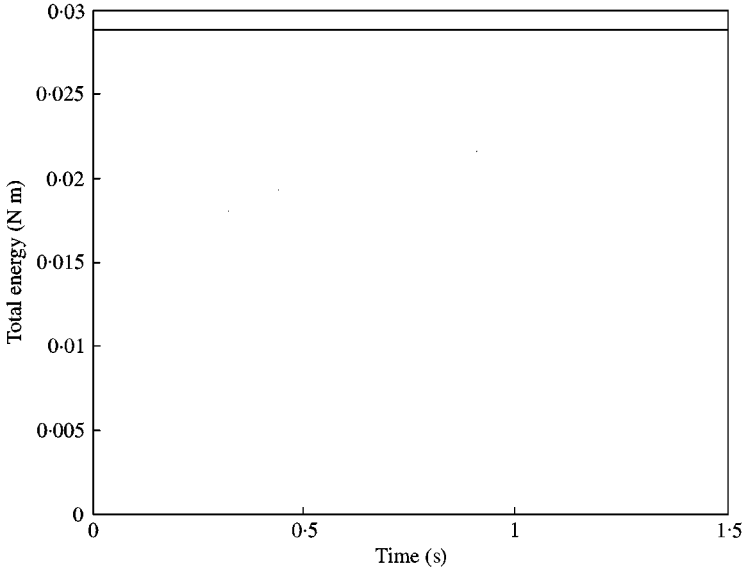

Figure 27. The total energy of the system for IC_1.

4.2. THE FREE RESPONSE WITH DAMPING

In this section, the response of the beam in still water is considered. As in the free vibration case, we examine the displacements at the tip, corresponding spectral density plots, the physical elongation, and the distribution of kinetic and potential energies.

4.2.1. *The displacements, phase plots, and spectral density plots for the free end motion*

The axial force is given by equation (27) and the transverse force by equation (28). The tip displacements with time and phase plots for the tip are shown in Figures 28–31 for the same four sets of initial conditions used for the undamped cases. Let us first consider responses obtained using the first three sets of initial conditions.

The frequencies of vibration vary with initial conditions as in the free responses. The tip transverse displacements when IC_1, IC_2 and IC_3 are used are plotted in Figure 32 for an easy comparison. The fundamental frequencies for the transverse response are about 1·08 Hz (0·93 s) when IC_1 and IC_3 are used, and 1·12 Hz (0·89 s) when IC_2 is used. When the periods of damped motion are compared with those of the corresponding free cases, damped responses are slower than undamped responses as we expected. It is interesting to note that the IC_2 produces the fastest response for both undamped and damped cases.

The fundamental frequencies of the corresponding tip axial displacements in Figures 28(a)–30(a) are twice those of transverse vibration as we have seen in the free undamped case.

Figure 33 shows the spectral density plots when IC_2 is used. The peaks occur at $f_u = 2{\cdot}24$, 32·5, 677, 2300, … (Hz), $f_v = 1{\cdot}12$, 33·6, 114, 247, 429, 564, 650, 677, 688, 711, … (Hz). When compared with the spectral density plots for the free vibration in Figure 14, peaks in Figure 33 generally are shifted to the left, some more so than others.

The transverse motion in all cases in Figures 28(b)–30(b) approaches its asymptote at zero by oscillating around it. However, the axial motion approaches its asymptote oscillating (at twice the fundamental frequency of the transverse motion) without

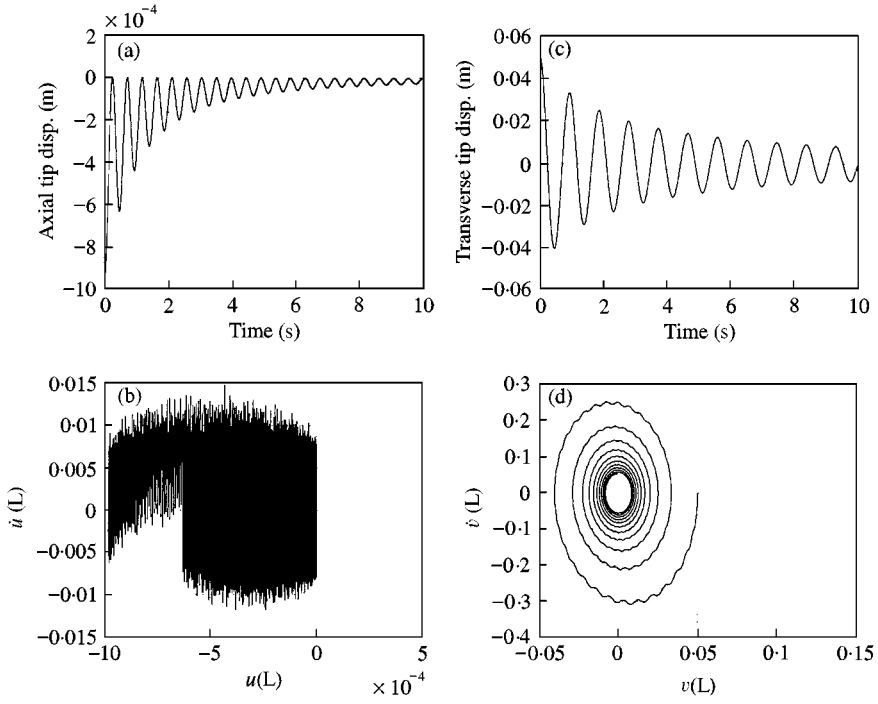

Figure 28. The damped free response plots using IC_1: (a) axial tip displacement versus time, (b) phase plot for the tip axial motion, (c) transverse tip displacement versus time, (d) phase plot for the tip transverse motion.

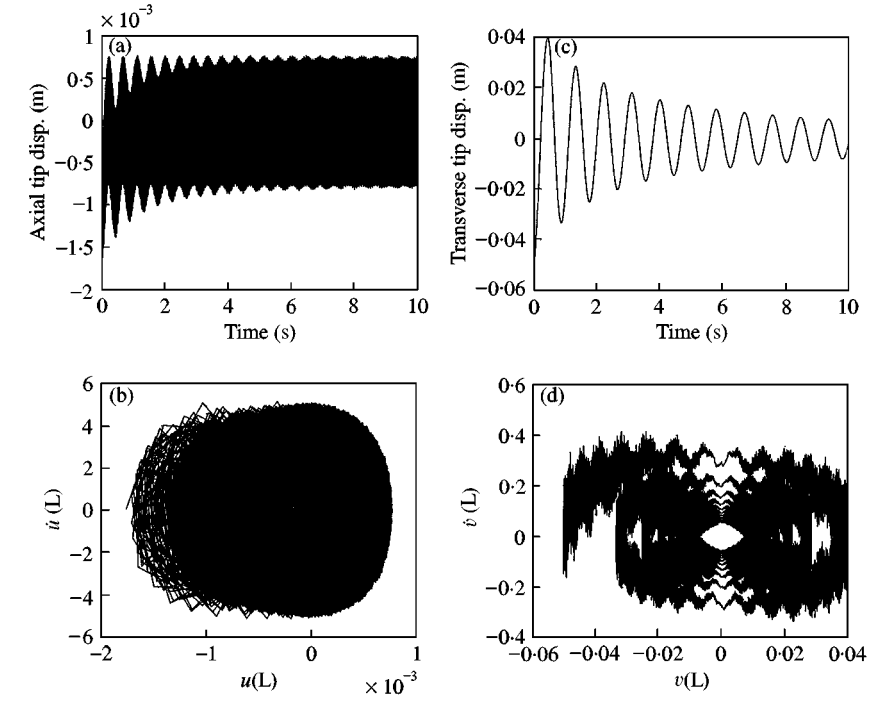

Figure 29. The damped free response plots using IC_2: (a) axial tip displacement versus time, (b) phase plot for the tip axial motion, (c) transverse tip displacement versus time, (d) phase plot for the tip transverse motion.

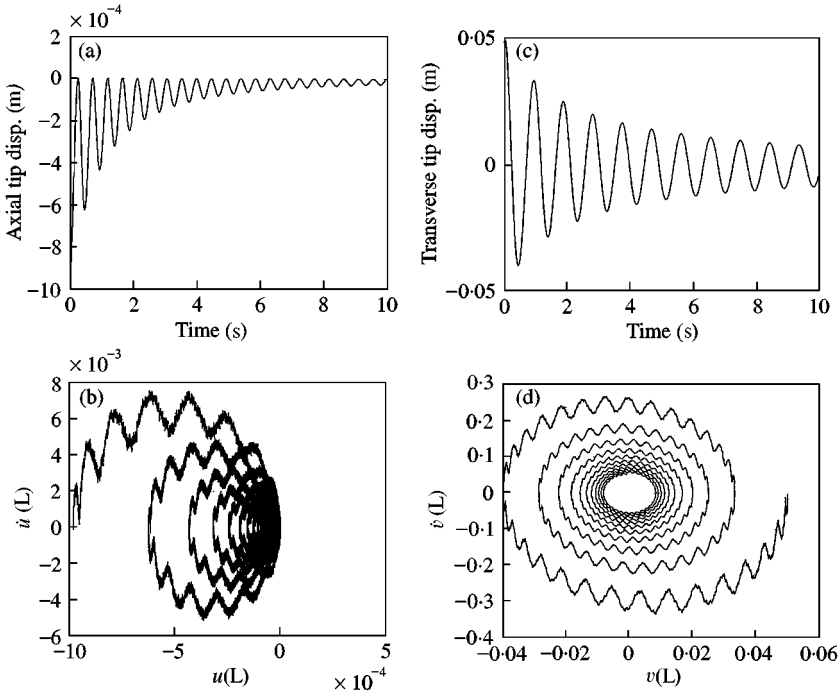

Figure 30. The damped free response plots for IC_3: (a) axial tip displacement versus time, (b) phase plot for the tip axial motion, (c) transverse tip displacement versus time, (d) phase plot for the tip transverse motion.

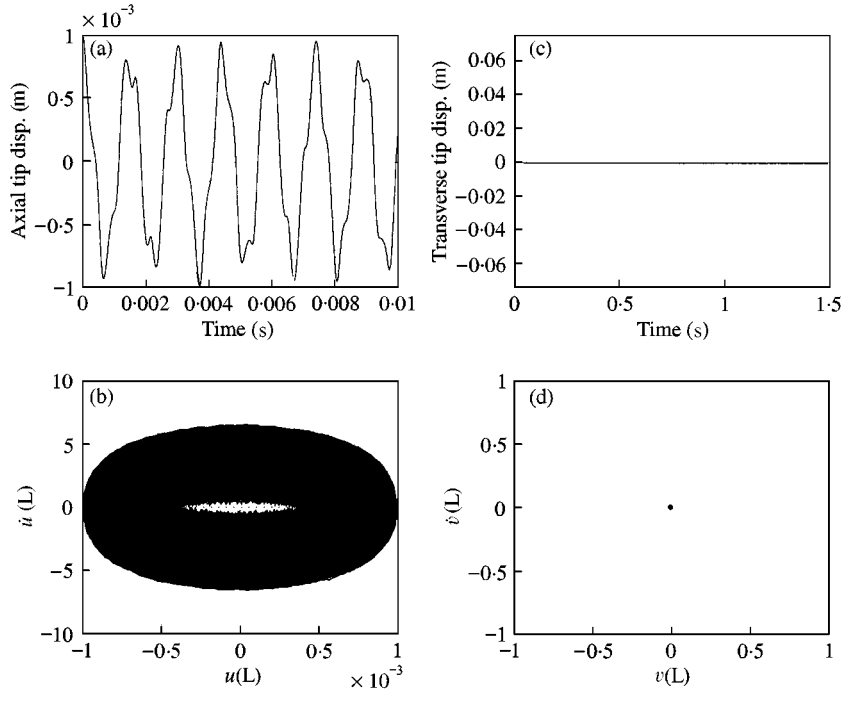

Figure 31. The damped free response plots for IC_4: (a) axial tip displacement versus time, (b) phase plot for the tip axial motion, (c) transverse tip displacement versus time, (d) phase plot for the tip transverse motion.

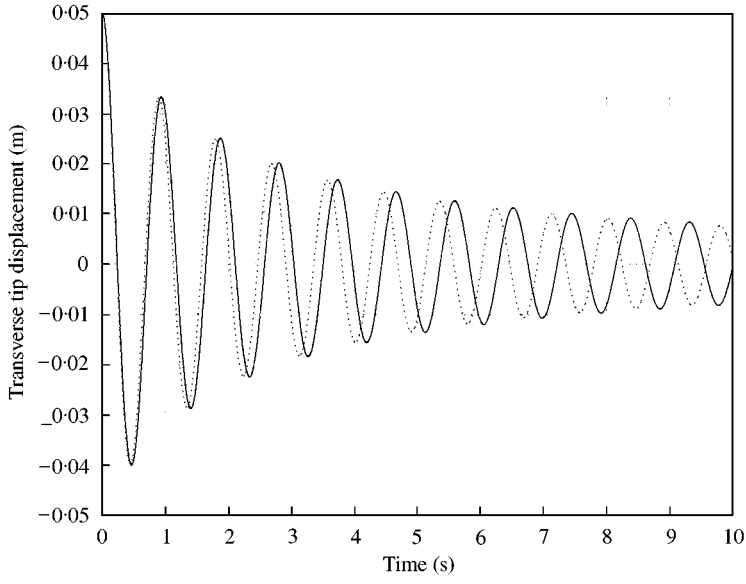

Figure 32. Transverse tip displacements of damped-free vibrations: —, IC_1; ·····, IC_2; – · – IC_3.

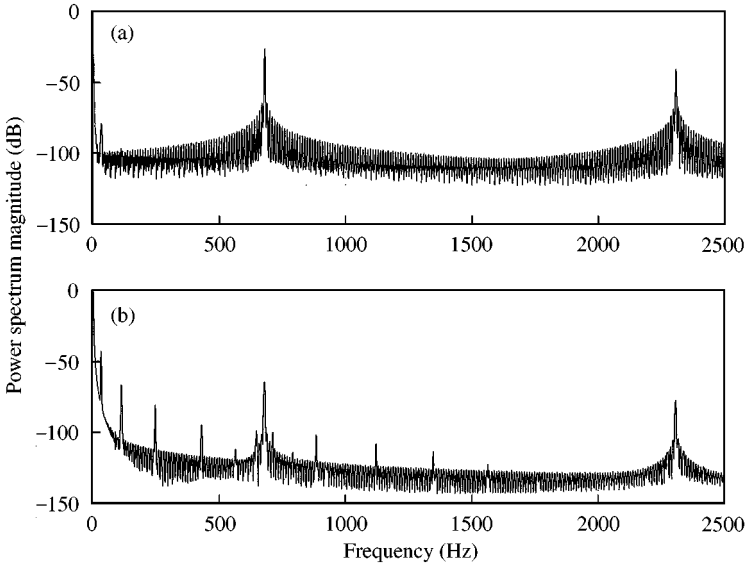

Figure 33. The power spectral density plots for the damped system using IC_2: (a) axial motion, (b) transverse motion.

overshooting the asymptote. It is helpful to recall that the axial displacement is the displacement from the reference configuration in the axial direction (x direction), and the axial motion at the fundamental frequency is geometrically induced from the transverse motion. Therefore, the axial displacement should not overshoot.

The axial displacement plots show that the fundamental frequency motions damp out and only the high-frequency response remains. After a while, the axial motion seems to be decoupled from the transverse motion. In order to examine why this happens, it is noted

that the Morison equation, is formulated to act perpendicular to the beam. We assumed that the rotation is small enough so that the Morison force only acts in the transverse direction. Therefore, the Morison fluid force directly affects the transverse motion, and affects the axial motion indirectly through the coupling of the transverse and the axial motions. The magnitude of its influence on the axial motion depends on the magnitude of the transverse motion and the coupling.

The Morison force in our case damps the transverse motion and therefore weakens the coupling between two motions. In the end, the axial motion becomes effectively decoupled from the transverse motion and the Morison fluid forcing. At this point, there is no mechanism for the fluid forces to slow down the axial motion. Since the transverse motion has exponentially decayed, we no longer see the fundamental frequency response in the axial motion.

Analytically, the change in total energy between $t = \tau_0$ and τ is given by

$$E(\tau) - E(\tau_o) = \int_0^L \left[\int_{\tau_0}^{\tau} \{C_D \rho_f r_o (\dot{u}v' - \dot{v})|\dot{u}v' - \dot{v}| + C_A \rho_f \pi r_o^2 (\ddot{u}v' - \ddot{v})\} \dot{v} \, \mathrm{d}t \right] \mathrm{d}X. \quad (43)$$

If there is no transverse vibration, $\dot{v}(X, t) = 0$, there is no energy loss. Therefore, it is possible that the undamped axial motion can still exist after the transverse motion has died out.

The phase plots in Figures 28(c, d)–30(c, d), when the transverse motion exists, show decreasing spirals, which means that the system is dissipative.

Figure 31, when there is no transverse motion, shows that the influence of the fluid forcing and the coupling between the transverse and the axial motion no longer exist. The axial motion in this case can be described by the linear longitudinal model given in equation (36).

The physical elongation in Figure 34 seem to persist with time. This is the result of having an axial motion that does not damp out. The elongations in all cases barely show the effect of diminishing transverse motion.

4.2.2. *The potential and kinetic energies*

Figures 35–37 show the potential energies, and Figures 38–40 show the kinetic energies of the system for the first three initial conditions. The energies of the damped system show some of the same characteristics that we have seen in the free system: shapes of elongation resemble the shape of membrane energy, the potential energies themselves are in phase, the kinetic energies themselves are in phase, the potential energy and the kinetic energy are 180° out of phase. The degree of the high-frequency component in the response is similar to the corresponding responses in the free vibration.

Now, let us look at how the energy is transferred between the potential energy and kinetic energy. Looking at the potential energies, only the membrane energy persists with time while the bending and spring energy seem to diminish with time. Looking at the kinetic energies obtained using IC_2 and IC_3, membrane energy shows up as the translational kinetic energy of the beam and the kinetic energy of the point mass. They, the membrane energy, translational kinetic energy, and the kinetic energy of the point mass, all have axial displacement in common. This is consistent with our previous result that only the axial motion persists in the system when the Morison force is applied.

Figure 41 shows the total energies of the system with time for all three initial conditions. The total energy decays while oscillating when IC_1 is used. The total energy fluctuates due to the phase difference between the kinetic and potential energy. When IC_2 and IC_3 are used, the total energy does not seem to decrease. This is because the most energy is in the

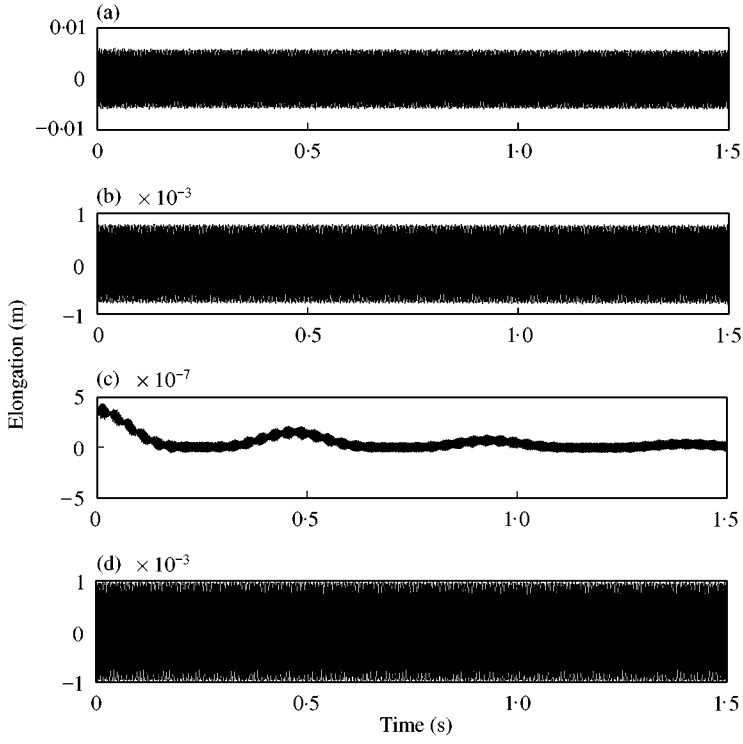

Figure 34. The elongation versus time for the damped free vibration using four sets of initial conditions: (a) IC_1, (b) IC_2, (c) IC_3, (d) IC_4. (The high frequency is at 677 Hz).

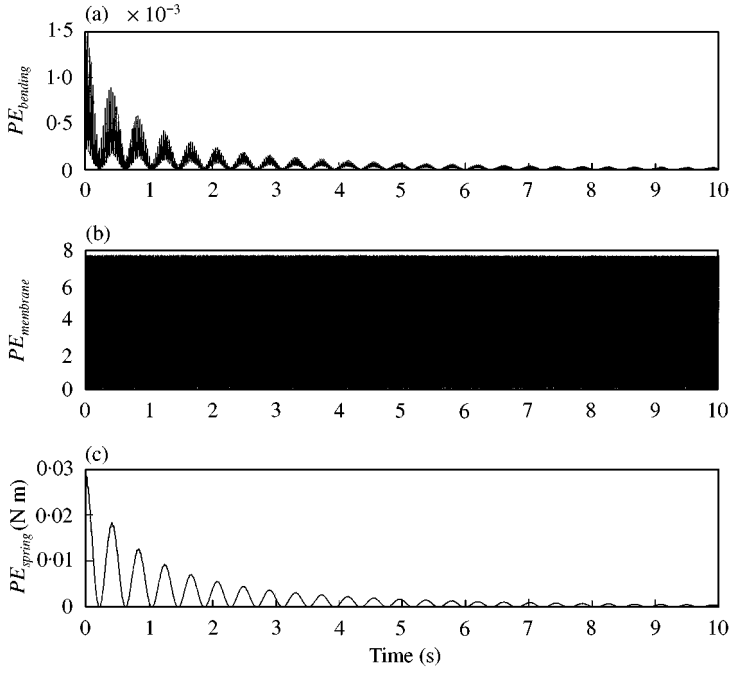

Figure 35. The potential energies of the damped free vibration using IC_1: (a) $PE_{bending}$, (b) $PE_{membrane}$, (c) PE_{spring}.

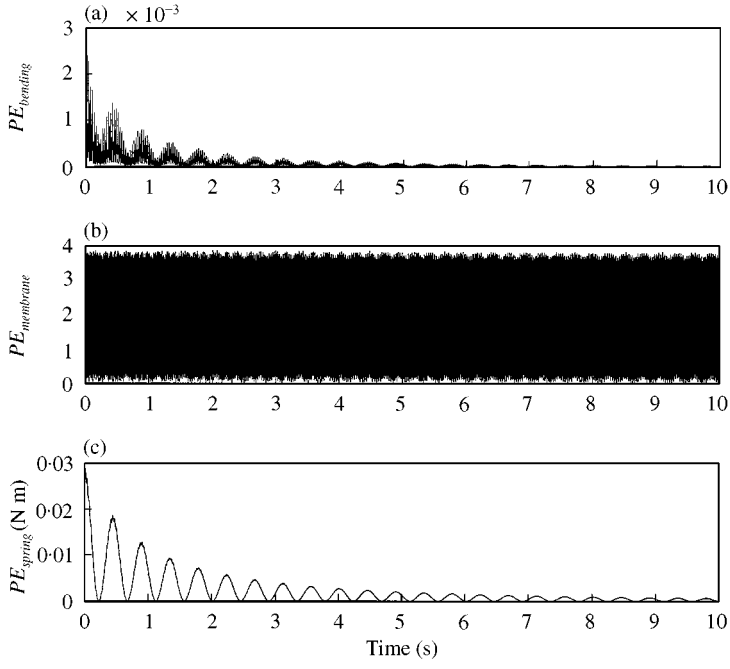

Figure 36. The potential energies of the damped free vibration using IC_2: (a) $PE_{bending}$, (b) $PE_{membrane}$, (c) PE_{spring}.

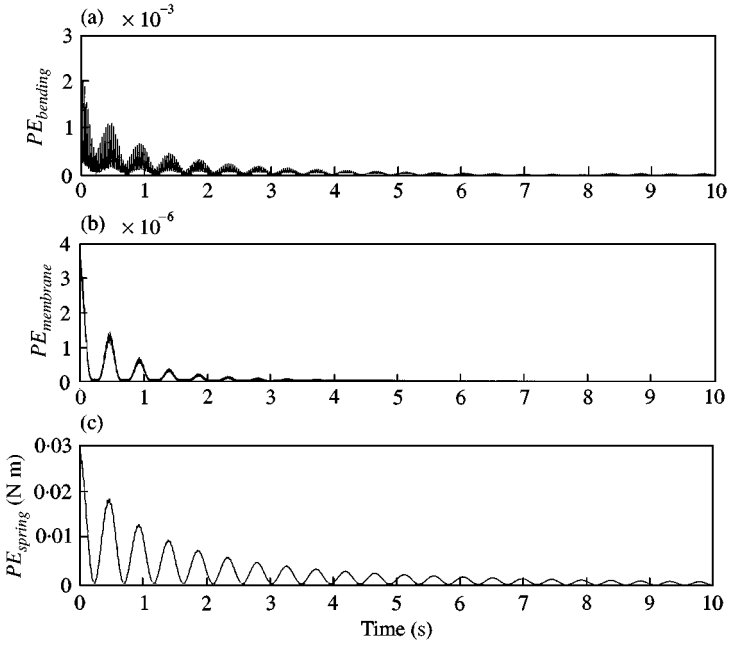

Figure 37. The potential energies of the damped free vibration using IC_3: (a) $PE_{bending}$, (b) $PE_{membrane}$, (c) PE_{spring}.

axial motion. Note that 50 and 100 nodes are used in order to produce energies associated with IC_2 and IC_3 respectively. This is because the error was noticeable when only 14 nodes are used in those cases.

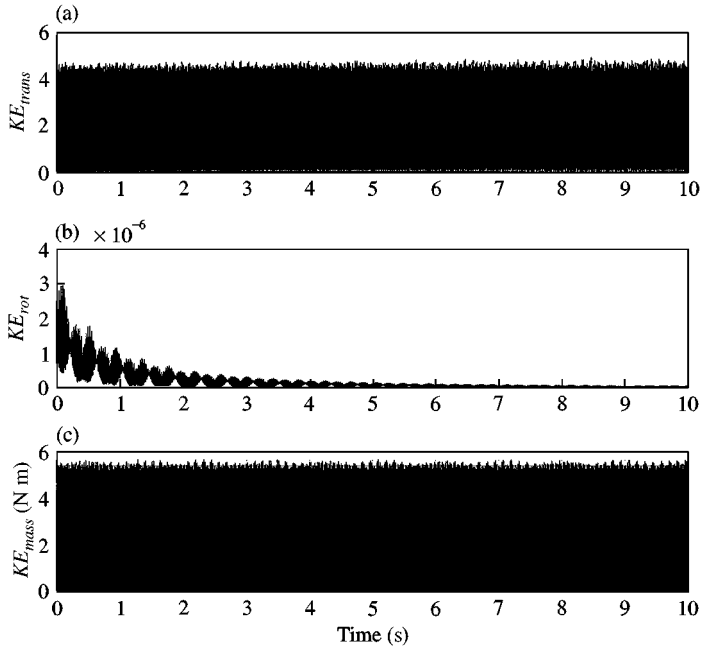

Figure 38. The kinetic energies of the damped free vibration using IC_1: (a) $KE_{translation}$, (b) $KE_{rotation}$, (c) $KE_{point\ mass}$.

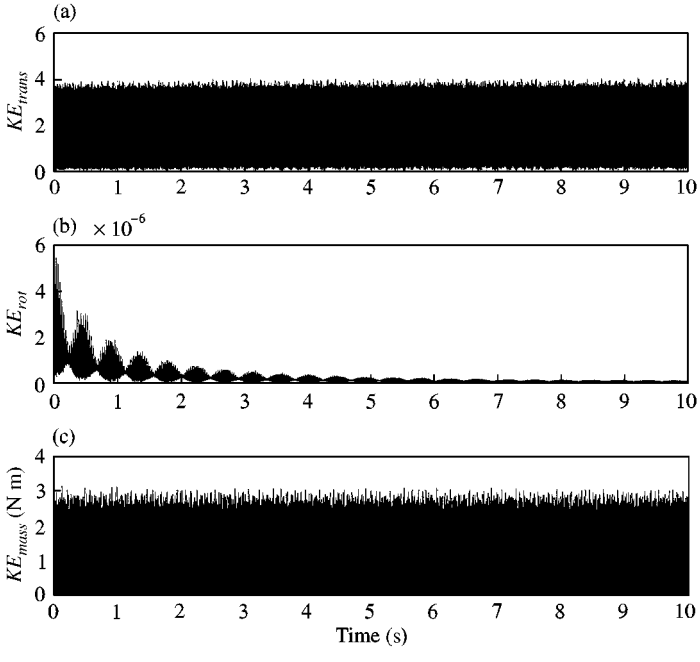

Figure 39. The kinetic energies of the damped free vibration using IC_2: (a) $KE_{translation}$, (b) $KE_{rotation}$, (c) $KE_{point\ mass}$.

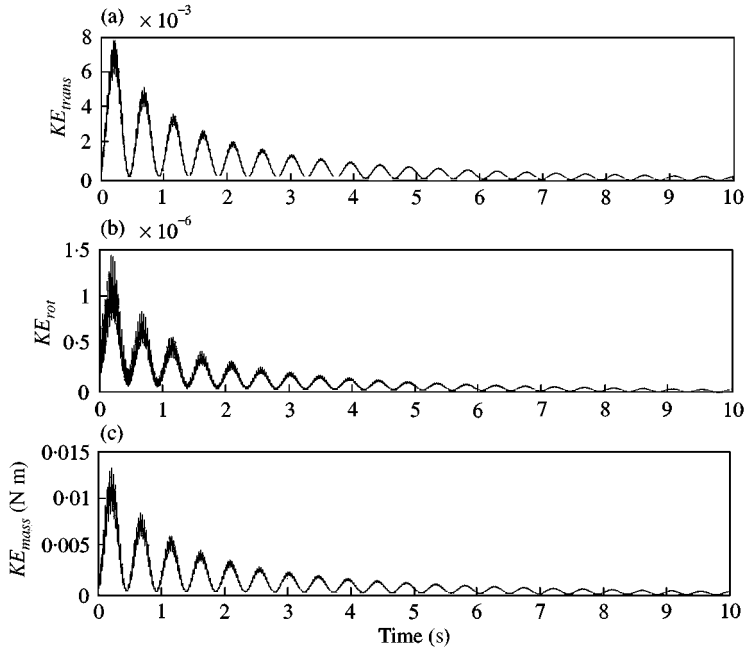

Figure 40. The kinetic energies of the damped free vibration using IC_3: (a) $KE_{translation}$, (b) $KE_{rotation}$, (c) $KE_{point\ mass}$.

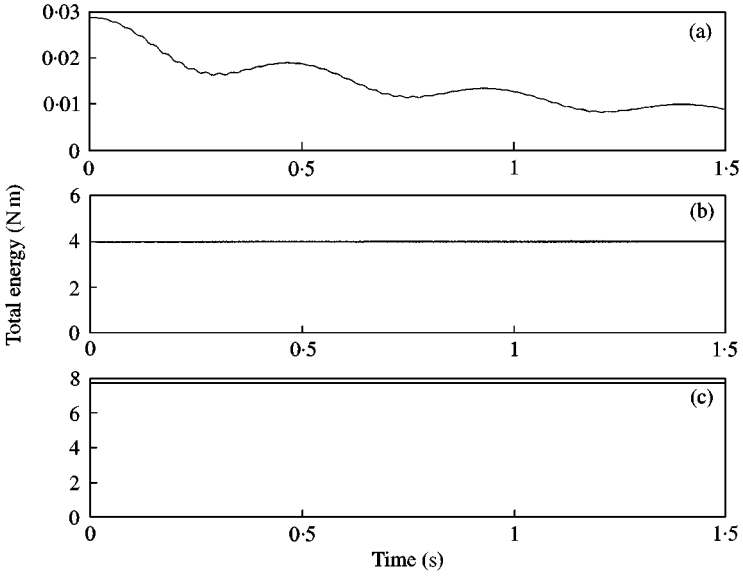

Figure 41. The total energy of the damped system: (a) IC_1 (14 nodes), (b) IC_2 (50 nodes), (c) IC_3 (100 nodes).

4.2.3. *Effect of varying fluid coefficients*

The added mass coefficient, C_A, changes the effective mass length density ($\rho A_{effective}$) of the beam. Therefore, larger C_A means longer period and smaller decay rate. Increasing the

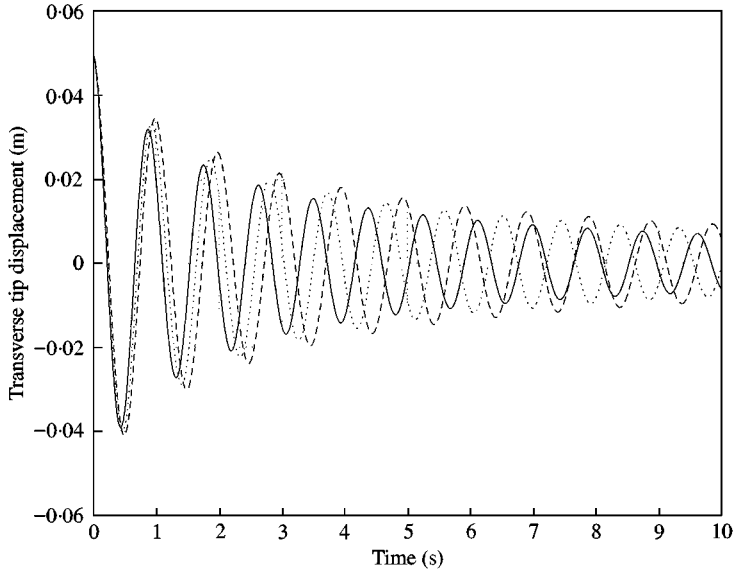

Figure 42. The transverse tip displacement using IC_1 and $C_D = 1$: —, $C_A = 0{\cdot}5$; ·····, $C_A = 1$; – –, $C_A = 1{\cdot}5$.

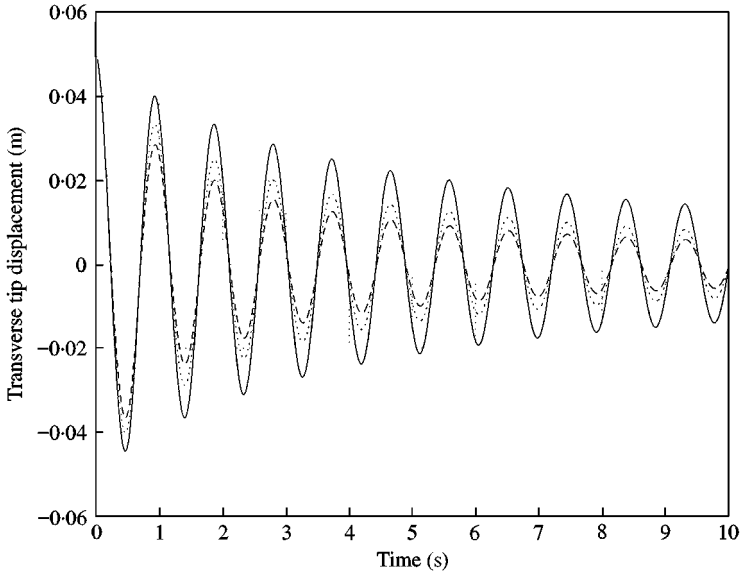

Figure 43. The transverse tip displacement using IC_1 and $C_A = 1$: —, $C_D = 0{\cdot}5$; ·····, $C_D = 1$; – –, $C_D = 1{\cdot}5$.

drag coefficient, C'_D, will increase the damping in the system. Here, the coefficients are varied $\pm 50\%$ of their nominal values of $C_A = 1$ and $C'_D = 1$.

Figure 42 shows the transverse tip displacement for $C_A = 0{\cdot}5$, 1, and 1·5. The periods of oscillation are 0·877, 0·933, 0·987 s. The amplitude ratios of the second to the first peaks are 0·640, 0·670, and 0·694. The period varied from $-6{\cdot}00$ to $+5{\cdot}79\%$, and the amplitude ratio varied from $-4{\cdot}48$ to $+3{\cdot}58\%$.

Figure 43 shows the transverse tip displacement for $C_D = 0{\cdot}5$, 1, and 1·5. The amplitude ratios of the second to the first peaks are 0·800, 0·670, and 0·570. The amplitude ratio varied from $+19{\cdot}4$ to $-14{\cdot}9\%$.

The responses are more sensitive to the drag coefficient than the added mass coefficient.

5. SUMMARY AND CONCLUSIONS

Analysis showed that the fundamental frequency for the free transverse motion ranged from 1·23 to 1·3 rad/s for the initial conditions used. The fundamental frequency for the transverse motion with damping ranged from 1·08 to 1·12 rad/s. The fundamental frequency of the axial motion was twice the fundamental frequency of the corresponding transverse motion. The axial motion at this frequency is geometrically induced from the transverse motion. It is possible to excite the axial motion without inducing the transverse motion, while the reserve is not possible. The fluid damping force modelled using the Morison equation affects the transverse motion directly, and then the transverse motion affects the axial motion through the system coupling. The influence on the axial motion by the Morison fluid forcing depends on the magnitude of the transverse motion.

ACKNOWLEDGMENT

This work is supported by the Office of Naval Research Grant No. N00014-97-1-0017. We would like to thank our program manager Dr Thomas Swean for his interest and financial support. The authors also are pleased to acknowledge the continued collaboration with our colleague, Professor Timothy Wei.

REFERENCES

1. R. ADREZIN, P. BAR-AVI and H. BENAROYA 1996 *Journal of Aerospace Engineering* **9**, 114–131. Dynamic response of compliant offshore structures—review.
2. S. M. HAN, H. BENAROYA and T. WEI 1999 *Journal of Sound and Vibration* **225**, 935–988. Dynamics of transversely vibrating beams using four engineering theories.
3. V. V. NOVOZHILOV 1953 *Foundation of the Nonlinear Theory of Elasticity*. Mineola, New York: Dover Publications Inc.
4. W. J. BOTTEGA 1986 *Dynamics and Stability of Systems* **1**, 201–215. Dynamic stability of support excited beam-column with end mass.
5. A. S. YIGIT and A. P. CHRISTOFOROU 1996 *Journal of Sound and Vibration* **196**, 617–627. Coupled axial and transverse vibrations of oilwell drillstrings.
6. R. ADREZIN and H. BENAROYA 1999 *Probabilistic Engineering Mechanics* **14**, 3–17. Response of a tension leg platform to stochastic wave forces.
7. R. ADREZIN and H. BENAROYA 1999 *Journal of Sound and Vibration* **220**, 27–65. Non-linear stochastic dynamics of tension leg platforms.
8. J. R. MORISON, M. P. O'BRIEN, J. W. JOHNSON and S. A. SCHAAF 1950 *Petroleum Transaction, AIME* **189**, 149–157. The force exerted by surface waves on piles.
9. J. WILSON 1984 *Dynamics of Offshore Structures*. New York: John Wiley and Sons, Inc.